ÅBO AKADEMI UNIVERSITY
FACULTY OF SCIENCE AND ENGINEERING

3D Printing of Inorganic Materials for Industrial Applications

Master's thesis
by
Valter Georgs

20.10.2023

Carried out at the Laboratory of Natural Materials Technology at Åbo Akademi University under the supervision of Professor Chunlin Xu and Docent Anna Sundberg.

Abstract

Georgs, Valter 3D Printing of Inorganic Materials for Industrial Applications

Master's thesis Laboratory of Natural Materials Technology, Faculty of Science and Engineering, Åbo Akademi University 2023, 76 pages, 47 figures, 4 tables, 1 appendix

Supervisors Professor Chunlin Xu and Docent Anna Sundberg at Åbo Akademi University.

3D printing of inorganic particles was first introduced in the 1990s, and since, multiple technologies have been developed for the purpose of printing inorganic structures. This thesis focuses on the possibilities and limitations of 3D printing of inorganic structures for industrial applications using the direct ink writing technology. The objective of this study was to prepare a shear-thinning and rapidly recovering printable paste with as high concentrations of inorganic particles as possible. Experimental methods involved preparation of different inorganic pastes, rheological evaluations of the different paste's behavior, 3D printing and post-processing of different structures, and evaluation of post-processed structures by visual and mechanical analyses.

Two different series of experiments were conducted in this thesis. In the first part a replication of a printable salt paste, as described in the article "3D Printing of Salt as a Template for Magnesium with Structured Porosity" by Kleger et al. (2019), was prepared, optimized, and printed to evaluate printability of a solids loaded paste. In the second part, the salt was replaced by a mixture of inorganic materials, and paste properties, printability, and quality of post-processed structures were evaluated. Another type of binder was also used in the inorganic pastes.

After exploring different components and approaches, a suitable inorganic paste which met the required rheological requirements was obtained. This paste allowed 3D printing of each collection of particle size available for this work. The initial pastes consisted of one collection of particles and two binders. As the particle size increased, issues regarding the printing process occurred as inconsistent extrusion. To overcome this issue, particles

of different sizes were incorporated in the paste, resulting in an even extrusion and improved flowability of pastes with larger particles present. The most promising structures contained approximately 75 wt-% of solids.

The printed structures were post-processed at elevated temperatures. For this process, graphite powder was used to allow free contraction of the structures as they shrunk, and to prevent the structures from sticking to the platform. Apart from a few unsuccessfully post-processed structures, most structures showed no signs of failure.

The post-processed structures were evaluated by different analyses, depending on components in the paste and structure design. DSC-TGA, SEM-EDS, and 4-point bending tests were performed on selected samples. Based on performance during processing and the results from post-processed structures evaluation, it can be concluded that a promising paste has successfully been developed for 3D printing of inorganic structures for industrial applications.

Keywords 3D printing, direct ink writing, surfactants, inorganic particles, rheology, particle size distribution

Acknowledgements

By this work I had the pleasure to work amongst a lovely group of people. I would like to express my gratitude to everyone involved in this project for all the support and help along the process.

I would like to thank my supervisors, Professor Chunlin Xu, for handing me this project and for the support and help with everything both related and unrelated to the project, and Docent Anna Sundberg, for the continuous support and help with the writing process. A special big thanks to laboratory assistant Oskar Backman, without whom I would never have made this much progress in the project. Thank you all for everything!

Lastly, I would like to thank my friends and family for their support and encouragement throughout my studies.

Turku, October 2023
Valter Georgs

Abbreviations

ABS	Acrylonitrile butadiene styrene
AM	Additive manufacturing
AOT	Bis(2-ethylhexyl) sulfosuccinate sodium salt
CAD	Computer aided design
DAC	Dual Asymmetric Centrifuge
DIW	Direct ink writing
DLP	Digital light processing
DMA	Dynamic Mechanical Analysis
DMD	Digital micro-mirror device
DSC	Differential Scanning Calorimetry
EDS	Energy Dispersive Spectroscopy
FDM	Fused deposition modelling
G'	Storage modulus
G''	Loss modulus
LOM	Laminated object manufacturing
LVE-region	Linear viscoelastic region
PA	Polyamide
PC	Polycarbonate
PLA	Polylactic acid
SDS	Sodium dodecyl sulfate
SEM	Scanning Electron Microscope
SLM	Selective laser melting
SLS	Selective laser sintering
TGA	Thermogravimetric Analysis
3DP	Binder Jetting
3ITT	3-interval thixotropy test

Table of Contents

Abstract I
Acknowledgements III
Abbreviations IV
Table of Contents V
1 Introduction 1
2 Theory 2
2.1 General background on 3D printing of inorganic materials 2
2.2 Slurry-based techniques 3
2.2.1 Direct ink writing 3
2.2.2 Digital light processing 4
2.3 Powder-based techniques 6
2.3.1 Binder jetting 6
2.3.2 Selective laser sintering 8
2.4 Bulk solid-based techniques 9
2.4.1 Laminated object manufacturing 9
2.4.2 Fused deposition modelling 10
2.5 Rheological aspects of DIW 12
2.5.1 Rheology measurements 14
3 Experimental 19
3.1 Salt structures I 19
3.1.1 Chemicals 19
3.1.2 Paste preparation 20
3.1.3 3D printing of salt paste 21
3.1.4 Sintering of salt green bodies 22
3.1.5 Rheology measurements 22
3.2 Inorganic structures II 23
3.2.1 Chemicals 23
3.2.2 Paste preparation 23
3.2.3 3D printing of inorganic paste 24
3.2.4 Post-processing of inorganic green bodies 25
3.2.5 Rheology measurements 25
3.3 Equipment 26
4 Results and discussion 30
4.1 Rheology measurements 30
4.1.1 Rheology measurements of salt paste 30
4.1.2 Rheology measurements of inorganic paste 37
4.2 3D printing and post-processing of salt and inorganic structures 41
4.2.1 3D printing and post-processing of salt pastes 41
4.2.2 3D printing and post-processing of inorganic pastes 42

4.3 Differential Scanning Calorimetry & Thermogravimetric Analysis 45
4.4 Scanning Electron Microscope & Energy Dispersive Spectroscopy 48
4.4.1 SEM-EDS of salt structures 48
4.4.2 SEM of inorganic structures 54
4.5 4-Point Bending mechanical strength test 56
5 Conclusions 61
6 Swedish summary – Svensk sammanfattning 63
7 References 68
8 Appendices 71
8.1 Appendix A – Rheology measurements of inorganic pastes 71

1 Introduction

3D printing is an additive manufacturing technique used to manufacture complex-shaped structures (Chen et al., 2019). Each structure is designed and sliced into 2-dimensional cross sections on a computer aided design program and printed according to the sliced sections one layer at a time. In the 1990s, 3D printing of inorganic particles was first introduced, and multiple technologies have since been developed for the purpose of printing inorganic structures.

3D printing enables preparation of tailor-made structures that are difficult to prepare by traditional fabrication methods and increases productivity as multiple structures can be produced simultaneously (Chen et al., 2019). Additionally, 3D printing offers solutions to different challenges associated with traditional fabrication methods, such as high cost, long processing times, and preparation of a variety of structures and geometries. One major challenge regarding fabrication of inorganic structures is to produce porous structures, which by conventional methods requires additional production steps (Zhang et al., 2022). While these methods remain challenging and time consuming, 3D printing emerges as a novel approach to overcome these challenges.

Direct ink writing is one of the 3D printing technologies capable of printing inorganic structures. This technology uses either pneumatic pressure, a piston, or a screw to extrude a viscoelastic paste or ink through a nozzle (Saadi et al., 2022). Since the technology relies on pressure-driven extrusion, the most crucial aspect is the rheological properties of the feedstock (del-Mazo-Barbara & Ginebra, 2021; Zhang et al., 2022). Ideally, the paste possesses a shear-thinning behavior to easily pass through the tiny nozzle, and a rapid recovery once the paste is extruded to guarantee structural stability and shape fidelity.

This aim of this thesis was exploring the possibilities and drawbacks of 3D printing of inorganic structures for industrial applications using the direct ink writing technology. Thus, it involves preparation and optimization of different inorganic pastes, rheological evaluations of the pastes, 3D printing and post-processing of different structures, and evaluation of post-processed structures by visual and mechanical analyses.

2 Theory

In the theoretical part of this thesis, additive manufacturing (AM) of inorganic materials with focus on structures that can be postprocessed in a later stage will be introduced. Since the work of this thesis was done using a direct ink writing (DIW) printer, this printing technique has received slightly more attention in comparison to the other 3D printing techniques introduced below.

2.1 General background on 3D printing of inorganic materials

3D printing technology is an AM technique used to manufacture physical parts in a point-by-point, line-by-line, or layer-by-layer manner (Chen et al., 2019). The objects are designed and sliced into 2D cross sections on a computer aided design (CAD) program and printed according to the sliced sections one layer at a time. 3D printing enables preparation of precise and demanding structures that are difficult to prepare by traditional fabrication methods and increases productivity, as multiple structures can be produced simultaneously. In addition to an increase in productivity, 3D printing offers solutions to different challenges associated with traditional fabrication methods, such as high cost, long processing times, and preparation of a variety of structures and geometries. One major challenge regarding fabrication of inorganic structures is to produce porous structures (Zhang et al., 2022). Conventional methods to produce these structures include gel and freeze casting, replica, direct foaming, sacrificial template, etc. While these methods remain challenging regarding the ability to produce porous complex structures or are complicated in procedure, 3D printing emerges as a novel approach to overcome these challenges.

3D printing of inorganic particles was first introduced in the 1990s (Chen et al., 2019). Since then, many 3D printing technologies have been developed for the purpose of producing inorganic structures. These technologies can be categorized based on the appearance of the pre-processed feedstock into slurry-based, powder-based, and bulk solid-based methods, which are listed with corresponding printing techniques in Table 1 below (Chen et al., 2019; Mamatha et al., 2022). Furthermore, the AM techniques are categorized into seven groups based on the form of feedstock used (Mamatha et al., 2022). These seven groups of additive manufacturing are classified as Material Extrusion, Material Jetting, Vat Polymerization, Powder Bed Fusion, Sheet Lamination, Binder

Jetting, and Direct Energy Deposition. The classifications are based on the feedstock's initial state, the application process, and the curing principle.

Table 1 Pre-processed feedstock with corresponding printing technique.

Feedstock	Printing technology	Abbreviateion
Slurry-based	Direct ink writing	DIW
	Digital light processing	DLP
Powder-based	Binder Jetting	3DP
	Selective laser sintering	SLS
Bulk solid-based	Laminated object manufacturing	LOM
	Fused deposition modelling	FDM

2.2 Slurry-based techniques

Slurry-based 3D printing techniques require feedstock in the form of pastes or inks (Chen et al., 2019). The feedstock is prepared by dispersing fine inorganic particles in liquid or semi-liquid systems and depending on the viscosity of the system and the solid loading the feedstock is categorized as either a paste or an ink. The slurry mixture can be printed by extrusion, photopolymerization, or inkjet printing. Commonly used 3D printing techniques that utilize slurry-based feedstock include direct ink writing, digital light processing, stereolithography, inkjet printing, and two-photon polymerization.

2.2.1 Direct ink writing

Direct ink writing is a 3D printing technique where a viscoelastic paste or ink is pressure-driven through a nozzle (Saadi et al., 2022). The printed structure is built in a layer-by-layer fashion by stacking filaments in desired shapes based on a CAD model (Chen et al., 2019; del-Mazo-Barbara & Ginebra, 2021). DIW is one of the mostly used AM techniques due to its ability to produce complex structures at low costs (del-Mazo-Barbara & Ginebra, 2021). The nozzles used for this technique range in size from as small nozzle diameters as 0.1 µm to several dm, depending on the attended application. Figure 1 illustrates the DIW technology.

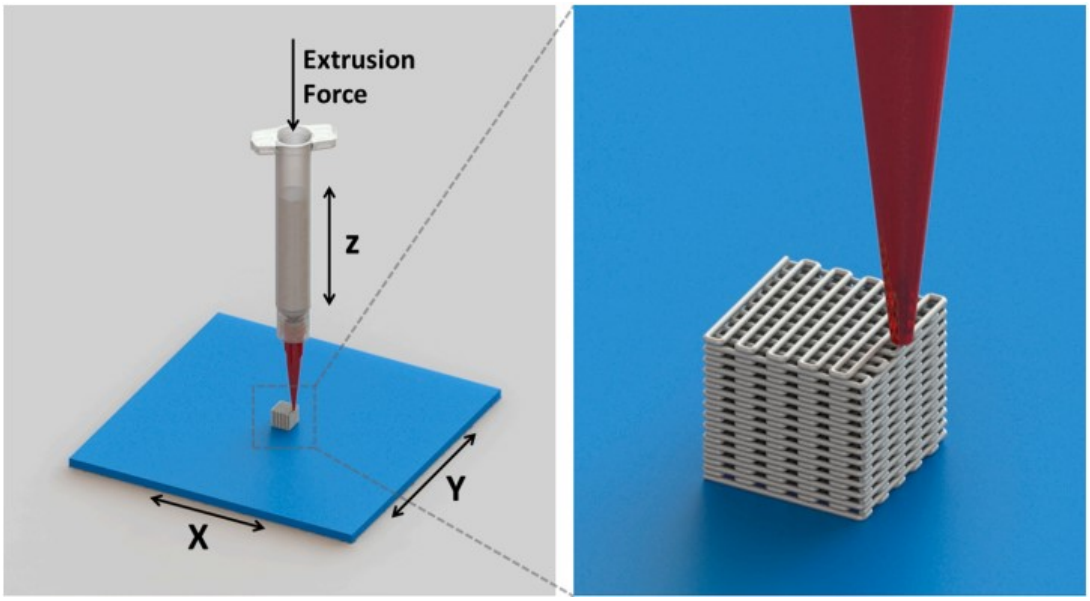

Figure 1 *Direct ink writing technology as a schematic illustration (del-Mazo-Barbara & Ginebra, 2021). The feedstock is extruded through a nozzle in a desired shape.*

The most crucial aspect of the DIW printing process is the rheological properties of the feedstock (del-Mazo-Barbara & Ginebra, 2021; Zhang et al., 2022). The paste requires appropriate rheological properties to be extruded through a tiny nozzle while simultaneously guaranteeing structural stability and shape fidelity when deposited. To obtain a stable structure the extruded paste needs to posess a shear-thinning behavior at variable flow rates (Saadi et al., 2022). With proper rheological properties met, the paste flows smoothly out of the nozzle without discontinuity of the extrusion or clogging due to particle jamming. Once deposited on the printing surface, the paste should idealy rapidly transition from a shear-thinning to a solid-like substance so that the structure can maintain shape fidelity. A more detailed description of the rheological requirements and properties regarding DIW is described in section 2.4.

2.2.2 Digital light processing

Digital light processing (DLP) is classified as a vat polymerization technique (Mamatha et al., 2022). A typical DLP system consists of a light source, a printing platform, and a tray for vat photo-curable precursor. During the printing process a light-curable resin stored in the vat is treated with a light source, either visible or UV-light, to solidify the resin through polymerization reactions. The desired structure is designed on a CAD program and sliced into layers. Each layer is projected as a sectional image on the surface

of the resin, curing the whole section/layer simultaneously. When a section is cured, the platform moves, and the next sectional image is projected on the resin. The projected image of a layer is an assembly of light and dark pixels created by micron-sized mirrors on a digital micro-mirror device (DMD) (Chaudhary et al., 2022). This device determines the resolution of the polymerized layer on the XY-plane.

There are two types of DLP system configurations, which are top-down and bottom-up (Mamatha et al., 2022; Chaudhary et al., 2022). This refers to the movement of the building platform. In the top-down approach, the platform is submerged in the resin and the light source is fixed at the top. The depth of the submerged platform equals the thickness of one printed layer. After a layer is cured the platform moves down so that the next layer can be cured on top of the previous one. The bottom-up approach has the light source in the bottom and the platform on top. The platform is immersed in the resin at a distance of one layer from the bottom of the vat container, allowing the light source to cure a layer on the platform by passing through the bottom of the container. Once a layer is cured the platform moves up for the formation of the next layer. The different DLP system configurations are shown in Figure 2.

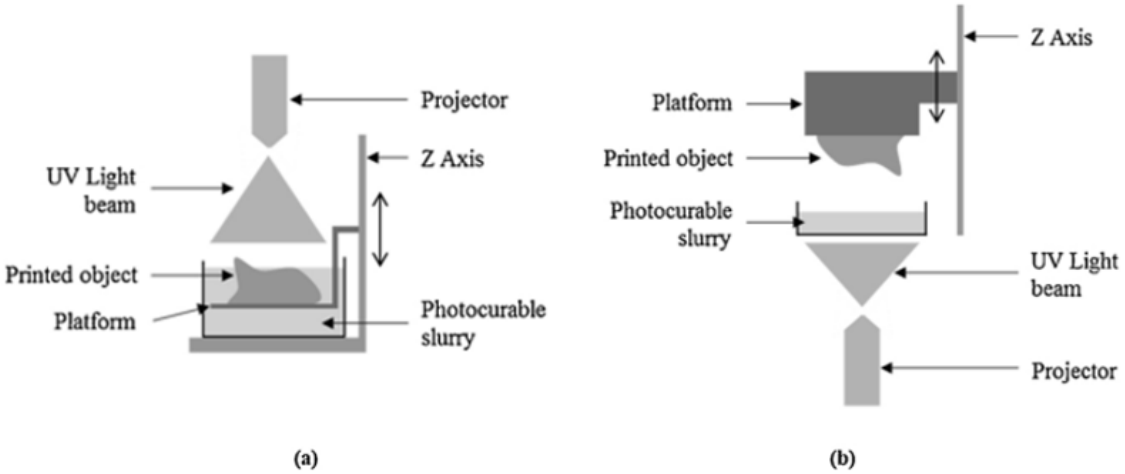

Figure 2 *Schematic illustration of* ***a)*** *top-down and* ***b)*** *bottom-up system configurations of a DLP printer (Santoliquido et al., 2019).*

The two configurations have their own advantages and disadvantages (Chaudhary et al., 2022). The bottom-up approach does not require as much fresh resin in the vat and can print small structures with a small amount of resin in the container. As the solidified layer is pulled up from the bottom of the container a vacuum develops, aiding the resin to recoat the bottom and allowing printing of more viscous resins. The critical aspect of this process, also considered a disadvantage, is the separation of the polymerized layer from the bottom of the vat container. To overcome this adherence, flexible and coated films, and separation movements have been introduced. On the contrary, the top-down approach does not encounter challenges with separation during the printing process. Simultaneously, this causes other issues as the polymerization occurs at the free surface in contact with air, which may affect the polymerization. Additionally, resins with lower viscosities are required for the top-down approach unless the printer is equipped with a scraper/re-coater to aid the coating of the printed structure.

2.3 Powder-based techniques

Powder-based techniques utilize loose particles as feedstock (Chen et al., 2019). Structures of inorganic particles can be produced by either binding the particles together with a liquid binder, or by selectively sinter or melt targeted areas of the powder with a powerful laser beam. Common 3D printing techniques that use powder-based feedstock are binder jetting, selective laser sintering, and selective laser melting.

2.3.1 Binder jetting

Binder jetting uses powdered feedstock and a printable binder to build 3D structures (Ziaee & Crane, 2019). There are several potential advantages of using binder jetting, as it can incorporate functionally graded materials and work with a wide variety of different powders. Compared to other AM techniques, binder jetting systems have a relatively high build rate due to only printing a binder, which is a fraction of the structure’s total volume.

During the printing process, the powdered feedstock lies in a powder bed onto which a liquid binder is sprayed. The application of the binder is controlled by a CAD program, creating one 2D layer at a time by gluing the powder particles together. Once a layer is

complete, a new layer of powder is applied onto the previous layer with a powder spread roller (Ziaee & Crane, 2019; Chen et al., 2019; Zhang et al., 2022). Figure 3 below shows the binder jetting process. Unbound powder acts as support for the printed structure during the process, allowing internal objects to be formed within the structure (Ziaee & Crane, 2019). Some binder jetting systems use heaters to control curing and moisture, but the heating is not a requirement for the process.

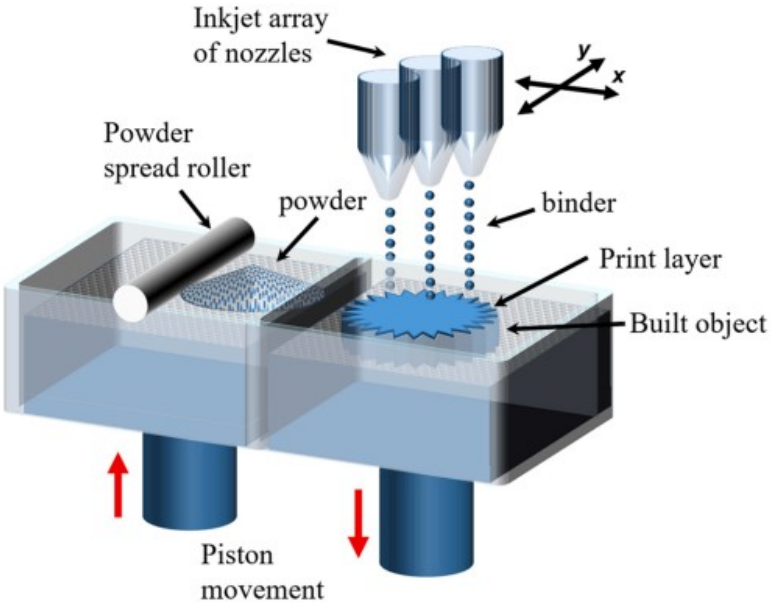

Figure 3 *Illustration of the binder jetting process. Once a layer is complete, the powder spread roller applies a new layer of powder on top of the previously formed layer until the structure is complete (Zhang et al., 2022).*

Porous structures containing inorganic particles can be produced with various binders, forming powder-binder composites (Zhang et al., 2022). Binder jetting as a technique is suitable for the production of porous inorganic structures, as the powder bed is porous in nature. Although the porosity is enhanced by the porous nature of the powder, the porosity of the final structure will significantly depend on the binder, the post-processing strategy, and the characteristics of the powder, such as shape, size, distribution, and composition.

2.3.2 Selective laser sintering

Selective laser sintering (SLS) is a similar technique as binder jetting, with the difference that instead of using a liquid binder it uses a high-power laser beam to irradiate selected sections of the powder bed (Chen et al., 2019). The laser heats up the powder to temperatures where sintering occurs, forming the structure by bulk joining. Once a layer is complete, a new layer of powder is spread out across the surface of the structure and the process continues one layer at a time until the final structure is produced. As in binder jetting, the excess powder which is not sintered during the process acts as support for the structure. Some SLS printers are equipped with heating systems to aid the process and prevent crack formations by reducing thermal stresses (Chen et al., 2018). The SLS process is shown in Figure 4 below.

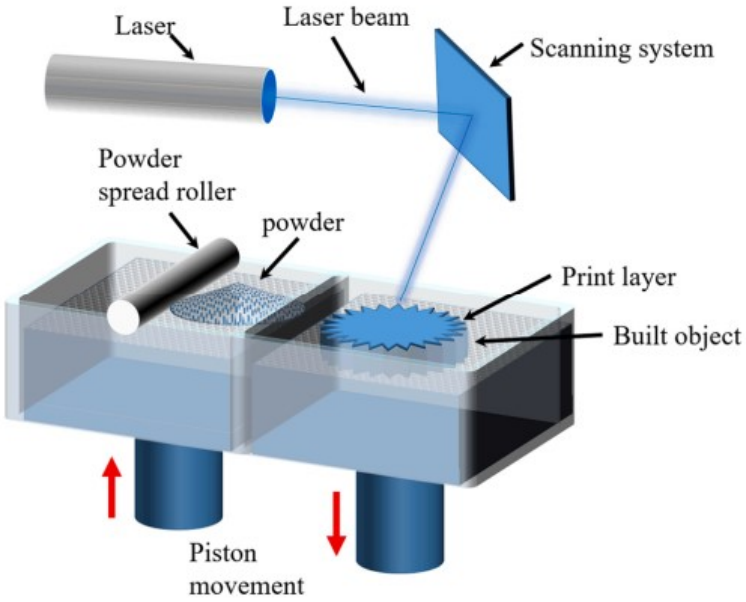

Figure 4 *Illustration of the SLS process. In comparision to Figure 3, many resemblances can be seen between the selective laser sintering and the binder jetting techniques, differing in the way of fusing the powdered particles together (Zhang et al., 2022).*

SLS of inorganic particles can be achieved by two different approaches, which are direct SLS and indirect SLS (Grossin et al., 2021). The direct SLS approach implies sintering of the powdered particles directly into the desired shape. To further densify the printed

structure, solid-state sintering or liquid-phase infiltration can be utilized as post-processing techniques. In the indirect SLS approach, a mixture of the powdered inorganic material and a sacrificial polymer binder is used. The sacrificial binder has a lower melting point and binds the inorganic particles, creating a green body of the desired geometry. By post-processing the green body with solid-state sintering or liquid-phase infiltration, the sacrificial polymer binder is removed and the inorganic structure densifies. Due to a high melting point of some inorganic materials, it is generally difficult to fabricate structures by direct sintering (Chen et al., 2018). Therefore, the alternative approach of indirect sintering is useful for materials with high melting points.

Regarding printing concept and process, selective laser melting (SLM) is identical to SLS (Hwa et al., 2017). The difference in the methods is that in the SLM technique the purpose is not only to sinter the particles, but to fuse them together by melting. The challenging aspect of this approach is melting inorganic particles with high melting points, but with an appropriate preheating process, complex structures with high strength and density can be manufactured.

2.4 Bulk solid-based techniques

3D printing techniques with the capability to print structures of inorganic materials and utilizes bulk solid-based feedstock are laminated object manufacturing and fused deposition modelling (Chen et al., 2019).

2.4.1 Laminated object manufacturing

The additive manufacturing process of laminated object manufacturing (LOM) consist of layer adhesion and shape cutting using a computer-controlled blade or laser (Chen et al., 2019; Dermeik & Travitzky, 2020; Zhang et al., 2022). During the process, a pre-processed sheet of desired printing material is continuously fed over the printing platform. With the aid of either a laser or a blade each layer of the desired structure is cut out into the right shape. As the process progresses a new layer of the sheet is applied on the previously cut structure, laminated to the surface, and cut out in accordance with the design of the layer. The bonding and lamination of each layer is conducted with heating and mechanical pressure. Figure 5 illustrates the LOM process.

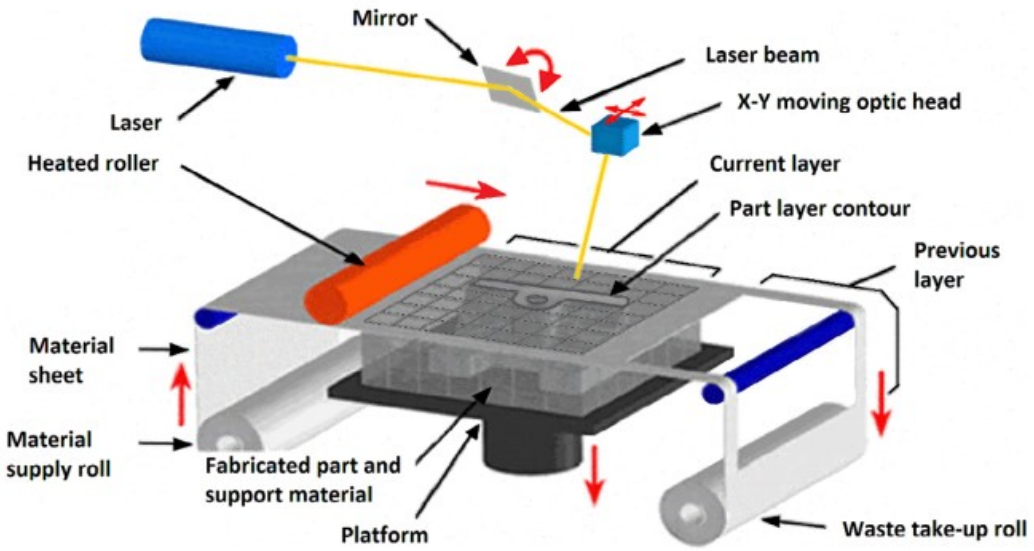

Figure 5 *Illustration of LOM process. The material sheet is fed over the printing surface where it is fused onto the structure and cut in a desired shape. When a layer is complete a new part of the sheet is fed on top of the structure, adhered with heat and pressure, and cut out in the right shape (Dermeik & Travitzky, 2020).*

LOM structures consisting of inorganic materials are usually built up from paper or polymer sheets filled with a high content of inorganic particles (Dermeik & Travitzky, 2020). When the structure is complete, a heat treatment step aids the removal of any organic components, resulting in an inorganic green body. The green body is then sintered at elevated temperatures to consolidate the structure. Structures manufactured by the LOM technique are typically dense and has low porosity, but through de-binding and sintering pore spaces can be obtained at the sites of burnt-off organic materials.

2.4.2 Fused deposition modelling

Fused deposition modelling (FDM) typically uses feedstock in the form of a filament (Chen et al., 2019; Vyavahare et al., 2020). The filament is pushed forward by rollers, and fed through a heated printhead where it melts. The printhead moves accordingly to the structure designed on a CAD program, depositing the melt in the XY plane through a small nozzle. Once a layer is complete, the printing platform moves down or the printhead

moves up precisely the distance of one layer height, and the following layer is deposited on top of the previous one. In Figure 6, the FDM process can be seen. The quality of the printed parts depends on feedstock quality and process parameters (Chen et al., 2019). For instance, homogeneity, dimensional accuracy, surface roughness, and mechanical properties highly depend on the width of the filament, building orientation, and layer thickness among others.

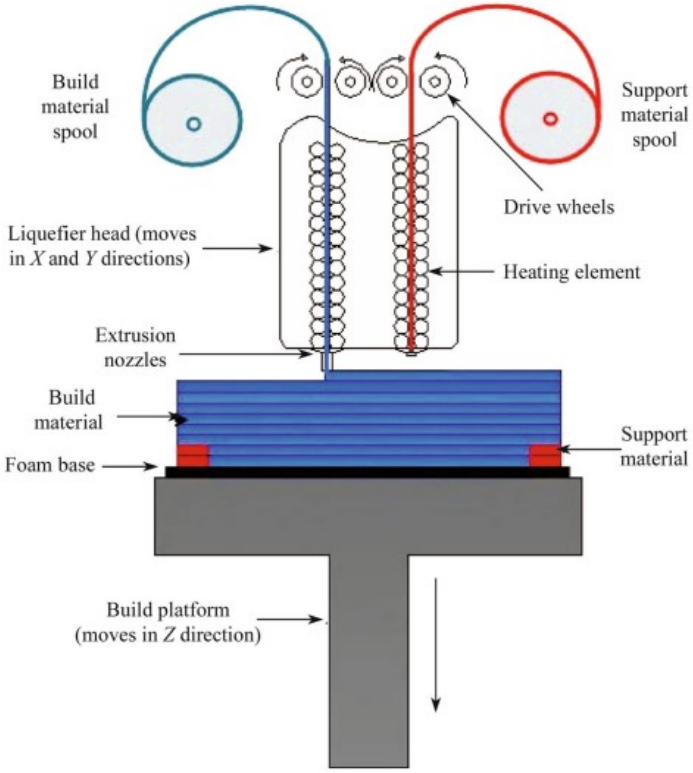

Figure 6 *Schematic illustration of the FDM process. As seen in the image, multiple materials can be extruded on the same structure with a printhead equipped with multiple extruders. Additional materials are often used as support while printing the structure (Mohamed et al., 2015).*

Typically used materials for FDM 3D printing are thermoplastic polymers e.g., acrylonitrile butadiene styrene (ABS), polycarbonate (PC), polyamide/nylon (PA), and polylactic acid (PLA) (Chen et al., 2019). As this method requires flexible and windable filaments as feedstock, the choice of materials is somewhat limited. However, composite filaments can be produced by loading solid particles into suitable binders, such as

thermoplastics. By incorporating particles into the filament, FDM can be utilized to print structures containing inorganic particles. The printed structure is then a green body which can be post-processed to remove the binder and achieve proper densification through sintering.

Printing with filaments containing inorganic particles has numerous factors that affects the process, including particle size and distribution, dispersity in the filament, the ratios between particles, binders, and additives, and the viscosity of the filament when extruded (Chen et al., 2019). To ensure a stable and continuous flow the inorganic particles need to be well dispersed and air entrapment within the filament should be minimal. Air entrapment can be decreased by degassing in vacuum and centrifugation.

2.5 Rheological aspects of DIW

The most crucial aspect in direct ink writing is the design of the feedstock, which is considered printable if it can be extruded as a continuous filament and make structures that are identical with the digitally designed model (Saadi et al., 2022). If the paste is properly prepared, a smooth flow without particle jamming or discontinuity is achieved, whilst a poorly prepared paste may have an uneven deposition, clog the extrusion nozzle, or fail to maintain the desired shape when deposited.

The ideal feedstock for DIW has shear-thinning properties, meaning that the material behaves like a fluid when extruded at high shear stresses but quickly exhibits an elastic behavior when the stresses cease and the paste is at rest (del-Mazo-Barbara & Ginebra, 2021). This behavior aids the flow of the feedstock, assuring extrudability even at lower extrusion pressures (Saadi et al., 2022). Typical viscosities for these inks/pastes range between 10^2 and 10^6 mPa s at shear rates around 0.1 s^{-1}. The transition from a more viscous-like fluid to a solid-like substance must occur rapidly once the paste is extruded to maintain shape fidelity of the structure. This ideal rheological response can be measured as the ratio between storage modulus (G') and loss modulus (G'') and gives an estimation on the feedstock's ability to maintain shape fidelity. Figure 7 illustrates the feedstocks behavior at different shear stresses when extruded through the nozzle. At rest G' is larger than G'' and the feedstock behaves solid-like. When shear stress is applied as the paste is extruded through the nozzle, G' drops below G'', causing a more viscous

behavior of the paste. Sites of applied shear stress is indicated in red (1), and sites of rest indicated in blue (2).

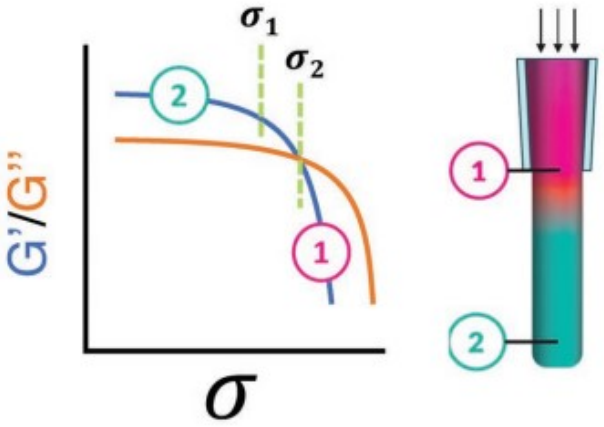

Figure 7 *Illustration of the flow behavior of a paste extruded through a nozzle. The shear-thinning paste flows when G'' is larger than G', while appearing solid-like at rest. Red (1) indicates sites where shear stress occurs, while blue (2) indicates a state of rest. The transition from a solid-like to a liquid-like substance occurs at the flow point (σ_2) (Saadi et al., 2022).*

The crossover point where G''/G' = 1 is called the yield point (Ang et al., 2023). During the extrusion of the paste, the applied shear stress (τ) must be larger than the yield point (τ_y) to achieve deformation and flow of the paste. With shear viscosity, the flow behavior can be determined, and the relationship between viscosity, shear stress, and shear rate can be described by a Herschel-Bulkley model. This model is shown below in equation 1:

$$\tau = \eta\dot{\gamma} = \tau_y + K\dot{\gamma}^n \qquad [1]$$

where (τ) is shear stress, (η) is apparent viscosity, ($\dot{\gamma}$) is shear rate, (τ_y) is the yield point, (*K*) is the viscosity parameter, and (n) is the power-law exponent.

The ratio G''/G' can be expressed as tan δ (δ = phase angle), which expresses the behavior of the material (Ang et al., 2023). If (δ < 45°), the material is solid-like, and if (δ > 45°), the material is liquid-like. Another useful rheological parameter is the yield stress (σ_y). Some materials have two different yield stresses, which are static yield stress (σ_y^{stat}),

indicating the minimum stress required to induce flow from rest, and dynamic yield stress (σ_y^{dyn}), indicating minimum stress required for continuous flow. With equation 2 below, the maximum shear rate induced in the nozzle when extruding the paste can be calculated:

$$\dot{\gamma}_{max} = \frac{4Q}{\pi r^3} \qquad [2]$$

where ($\dot{Q}$) is the volumetric flow rate, and $\dot{Q} = Sr^2$, where S is the printing speed and r is the nozzle radius. With these parameters, the printing settings can be optimized as the static and dynamic yield stresses provide information about the flowability of the paste, and the maximum shear rate provides information about how much shear the paste will be exposed to.

To maintain extruded shape and proper structure, it is desirable to use high yield stresses when extruding the paste (Ang et al., 2023). Simultaneously, high yield stresses and viscosities are the main reasons for cloggage of the nozzle. This is due to particle agglomeration that forms in the paste. By ball milling the paste, the particle size can be refined, and powder dispersion can be improved. Another reason for nozzle clogging is the usage of an unsuitable nozzle size (Coffigniez et al., 2021). If the nozzle diameter is too small for the paste, a less homogenous extrusion occurs, which in turn can result in arch formations within the nozzle.

2.5.1 Rheology measurements

There are many different rheology tests to obtain information about the rheological properties of the feedstock (del-Mazo-Barbara & Ginebra, 2021). With the aid of rotational or shear rheometers, shear stresses, strains, and rates can be applied to a sample using specific geometries to investigate these properties. The most commonly used geometries are concentric cylinders, cone-plate, and parallel plates. Usually, the tests are conducted in rotational or oscillatory mode, where in rotational tests the upper part of the geometry rotates in the same direction throughout the test, while in oscillatory test, the upper part oscillates sinusoidally with a precise frequency or amplitude. For highly viscous pastes, such as pastes loaded with high concentrations of inorganic particles for

direct ink writing, the most suitable geometry is the parallel plates. The gap between the plates can be modified, but it is recommended that the gap is at least 10 times larger than the largest particles in the paste.

Dispersions with high solids content tend to slip at the bounding surfaces of the geometries instead of deforming and flowing (Cloitre & Bonnecaze, 2017). This phenomenon is called wall-slip and can cause errors in different material properties determinations. If wall-slip occurs, the actual deformation and deformation rate experienced by the material differs significantly from the applied shear rate. To decrease the effect of wall-slip, different methods have been developed. For instance, specific geometries with textured surfaces are commonly applied to suppress wall-slip. These textured surfaces can be obtained by sandblasting or machining the surface of the geometries, or by applying sandpaper or creating grooves on the surface of the geometry. Perfect measurement conditions regarding the occurrence of wall-slip are hard to obtain, but a decreased effect of the slip improves the measurements significantly.

A flow curve measurement can be done to evaluate the sample's flow behavior (Anton Paar GmbH, 2023). A flow curve measurement is done by increasing shear rate stepwise with a defined measurement point duration while determining the respective shear stress at each step. The results from this kind of measurement can be displayed as diagram showing shear stress values, or as a diagram showing the corresponding viscosity function. Different flow behaviors, such as ideally viscous, shear-thickening, and shear-thinning can be identified by this measurement method. Figure 8 illustrates the flow curve settings and the flow curve response for a shear-thinning sample.

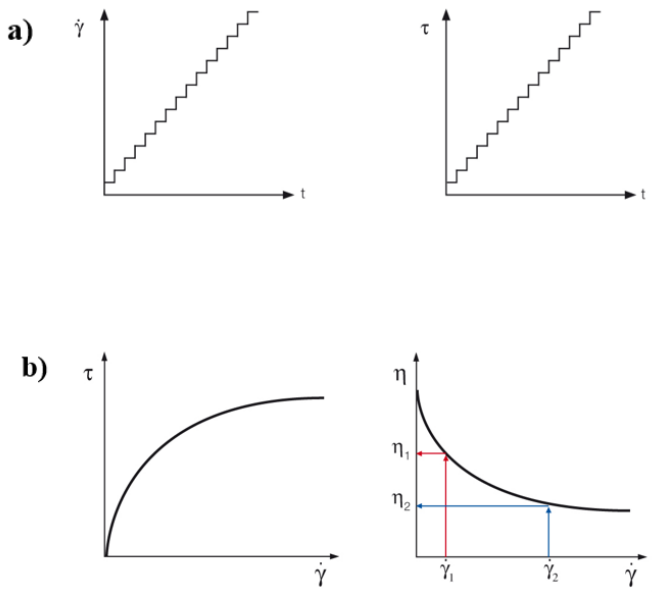

Figure 8 *a) Rheometer settings for a flow curve measurement (Anton Paar GmbH, 2023). b) The flow curve response for a shear-thinning material. As the material starts to deform, the shear stress decreases towards linearity as the shear rate increases. The same can be seen in the viscosity as the material becomes less viscous with an increasing shear rate.*

An amplitude sweep measurement is useful to describe the behavior of a material (Anton Paar GmbH, 2023). The measurement is done by stepwise increasing the deflection of the measuring system, while keeping the frequency constant. Either the shear strain or shear stress can be controlled for the measurement, depending on the user's preference for the measurement. The results from an amplitude sweep are often presented as a diagram with shear strain or stress plotted on the x-axis, and G' and G'' plotted on the y-axis. Figure 9 illustrates results from two amplitude sweep measurements of a gel-like/solid material and a fluid material.

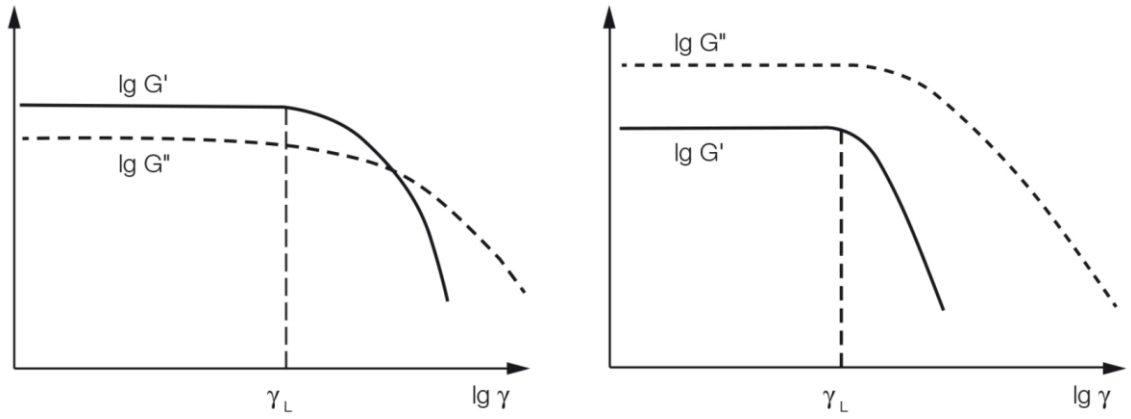

Figure 9 *Left: Amplitude sweep result for a gel-like/solid material (Anton Paar GmbH, 2023). In the linear viscoelastic region G' > G'', indicating a solid-like behavior. With additional strain/stress G'' becomes greater than G', indicating a more fluid-like behavior. Right: G'' > G' throughout the measurement. The material in question is thus a fluid.*

Evaluation of G' and G'' in the linear viscoelastic region (LVE-region) gives information about the sample's viscoelasticity (Anton Paar GmbH, 2023). The LVE-region is the range in which the measurement can be performed without deforming the structure of the material, the region with the lowest strain values. If G' > G'' in the LVE-region, the sample shows a solid or gel-like structure, while if G'' > G' the sample shows a fluid-like structure. When performing oscillatory tests, it is often required to perform them at stress or strain levels within the LVE-region. Therefore, an amplitude sweep must be performed first to evaluate this region when examining an unknown sample.

To gain a greater understanding of different samples behavior, both the storage and the loss modulus can be evaluated separately by investigating rises and slopes of the individual curves (Anton Paar GmbH, 2023). The stiffness or gel strength of a sample is represented by G' in the LVE-region. As the sample is deformed with increasing stress or strain values the curve drops down. If the decreasing slope of the curve is sharp, it indicates a brittle fracturing behavior where the sample does not break homogenously, while a more continuous decrease indicates a gradual breakdown of the structure. The portion of lost deformation energy is described by the values of G''. The G'' tends to show a quite linear curve in the LVE-region, after which an increase occurs in the slope until it reaches a maximum followed by a steep drop. Before reaching the maximum point,

a few non-linear points can occur in the LVE-region. This behavior is a result of micro cracks in the sample where small fragments of the structure may break. At the maximum point a continuous macro crack occurs, and the sample starts to flow. If this point is reached G'' dominates over G', as the crossover point where G' = G'' is exceeded.

In addition to the flow behavior of a sample, it is important to investigate how fast the deformation can be reversed (Anton Paar GmbH, 2023). This can be evaluated by performing a 3-interval thixotropy test (3ITT). The key requirements for a proper regeneration of a sample are that the regeneration is not too fast or too slow. If the regeneration is too fast, the leveling is poor, while a too slow regeneration may lead to sagging. The 3ITT test is usually done as a time-dependent controlled-shear-rate rotational test with three intervals. In the first and third interval, very low shear is applied to simulate the rest behavior of the sample. In the second interval, a strong shear is applied to simulate the samples structural breakdown. Figure 10 illustrates the principle of the test and a typically presented result from a 3ITT test.

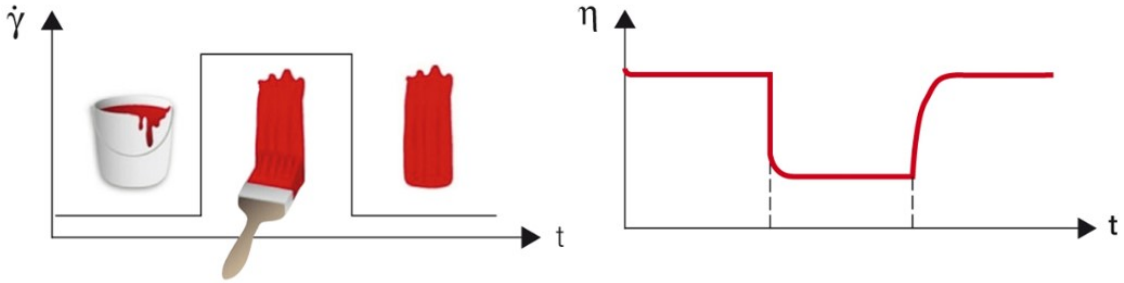

Figure 10 *Left: Illustration of the three intervals: rest – structural breakdown – rest (Anton Paar Gmbh, 2023). Right: Typically presented 3ITT test result. The result is often presented as a time-dependent viscosity function. As high shear is applied the viscosity decreases rapidly. When decreasing the shear, the sample gradually returns to its rest state.*

3 Experimental

This thesis was carried out in two parts. In the first part of the work, the article "3D Printing of Salt as a Template for Magnesium with Structured Porosity" by Kleger et al. (2019), was replicated to create a printable paste with a high salt content. In the second part of the work, the salt was replaced by an inorganic mixture, and the paste, printing parameters, and post-processing were optimized. In this chapter, these parts will be described along with equipment and materials used for the experiments.

3.1 Salt structures I

For the preparation of salt pastes, NaCl was used as salt, Sodium Dodecyl Sulfate (SDS) or Dioctyl Sulfosuccinate Sodium Salt (AOT) was used as surfactant, and Paraffin oil was used as binder. In the article by Kleger et al. (2019), 28.6 wt-% of Paraffin oil was used with different ratios of NaCl and SDS/AOT. Depending on surfactant used for the paste, the preparation method differed slightly as described in section 3.1.2.

3.1.1 Chemicals

The chemical structures of the chemicals used for the preparation of printable salt pastes are shown below in Figure 11, and their properties are shown in Table 2.

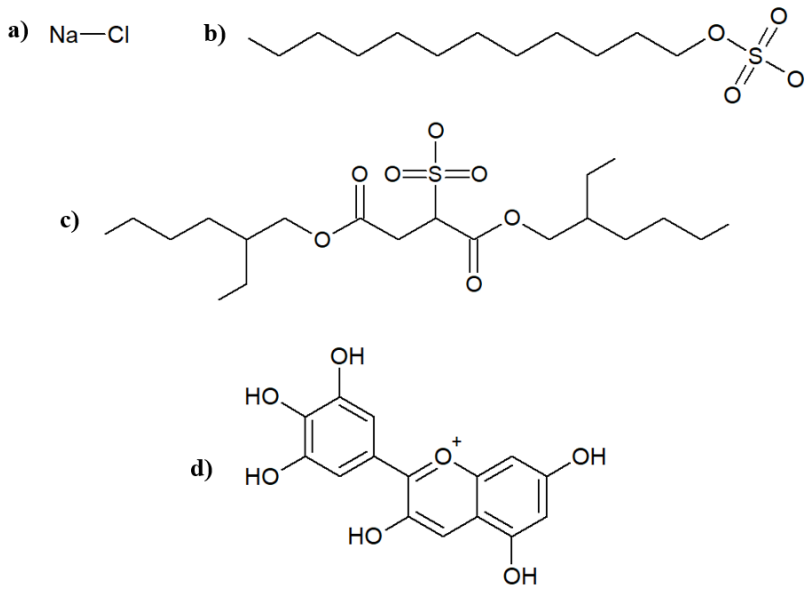

Figure 11 *Chemical structure of* ***a)*** *NaCl* ***b)*** *SDS* ***c)*** *AOT* ***d)*** *Paraffin oil.*

Table 2 Chemical properties of NaCl, SDS, AOT, and Paraffin oil.

Chemical	Density (g/cm^3)	Melting point (°C)	Molar mass (g/mol)
NaCl	2.165	801	58.44
SDS	0.37	204-207	288.38
AOT	1.146	173-179	444.56
Paraffin oil	0.88	N/A	N/A

3.1.2 Paste preparation

Preparation of SDS-containing salt paste

For the preparation of salt pastes containing NaCl, SDS, and Paraffin oil, the NaCl was ball milled to a fine powder to minimize the risks of nozzle clogging during printing. After obtaining a fine powder, SDS and Paraffin oil was added to the salt and ball milled to a smooth paste. For pastes containing SDS, 28.6 wt-% Paraffin oil was used in relation to the total mass of the paste. Amount of surfactant used refers to its mass percentage with respect to the amount of solids used. For instance, SDS10 was a paste with 28.6 wt-% Paraffin oil, 64.26 wt-% NaCl, and 7.14 wt-% SDS. Only considering the solids in this paste, the amount of SDS is 10%.

Preparation of AOT-containing salt paste

For the preparation of salt pastes containing NaCl, AOT, and Paraffin oil, the AOT was dissolved in Paraffin oil by magnetic stirring. Since the dissolving of the surfactant was time consuming, it was mainly done overnight. Identical to the above-mentioned method of SDS-containing salt pastes, the NaCl was ball milled to a fine powder and the mixture of AOT and oil was added to the salt and ball milled to a smooth paste. For pastes containing the surfactant AOT, a reduced amount of Paraffin oil was essential as the paste became too liquid-like with 28.6 wt-% Paraffin oil. Similar pastes were obtained with only 20 wt-% of Paraffin oil, and a much lower surfactant content. With lower contents of both the binder and the surfactant, pastes with much higher concentration of NaCl were obtained. As described above, the amount of Paraffin oil used refers to the total mass of the paste, while the amount of AOT used refers to the amount of NaCl used. As AOT allowed higher solids loadings than SDS, this surfactant was considered the best option for continuous experiments for both the salt paste and the inorganic mix paste experiments.

Once a paste was obtained through ball milling the contents, the paste was placed in an airtight container and stored in a ventilated cabinet to reduce the risk of water absorption from the environment. The paste was then either loaded into 10 ml syringes for 3D printing or used for rheology measurements.

3.1.3 3D printing of salt paste

Printing parameters were optimized for each paste by printing small-scale structures directly on a petri dish. During these optimization prints, printing pressure, printing speed, layer heights, and infill of the structures were changed to acquire as smooth and even extrusion as possible before printing the actual designs. Once optimized, the actual structures were printed directly on a filter paper. After completing the structures, they were covered with graphite powder to enhance drying by absorbing the Paraffin oil out of the object. As the structures had dried properly, they could be handled gently without breaking them. In Figure 12, a structure being printed directly on a filter paper can be seen.

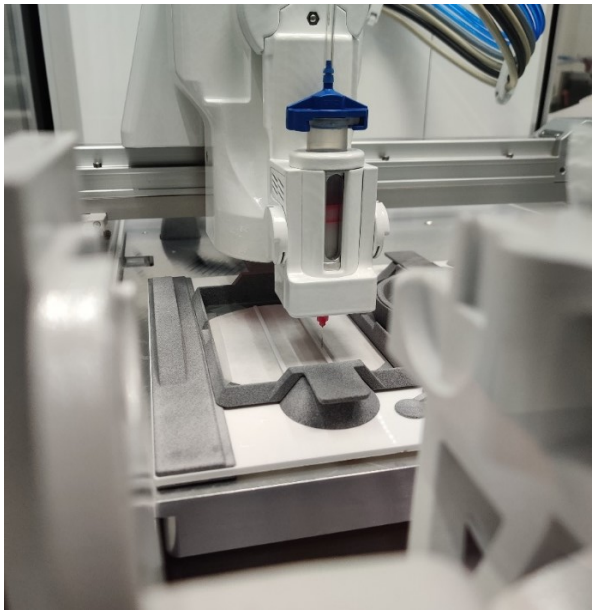

Figure 12 *Printing structures directly on a filter paper removed the need of moving structures to dry after the printing was complete. To enhance the absorption of Paraffin oil, the structures were covered with graphite powder.*

3.1.4 Sintering of salt green bodies

Once the printed structured had dried properly on a filter paper and were covered with graphite powder, they were sintered to remove the surfactant, the binder, and any organic impurities. For the sintering of salt structures, a sintering program as described in the article by Kleger et al. (2019) was used. The furnace used at Åbo Akademi University could not cool down at the rate that was set up. Therefore, there was a slight modification to the program as the cooldown occurred naturally from 690°C to room temperature. The setup for the program used is shown in Table 3 below.

Table 3 Sintering setup for salt structures (Kleger et al., 2019).

Temperature	Time (h)	Dwell time (h)	Reason
RT --> 200°C	2	2	Remove Paraffin oil
200°C --> 400°C	2	5	Decompose surfactant and residual Paraffin oil
400°C --> 690°C	5	3	Sinter NaCl particles
690°C --> RT	N/A	none	Cooldown

3.1.5 Rheology measurements

Different rheological measurements were conducted on salt pastes with different compositions to evaluate the flow and recovery behavior of the pastes. The measurements that were performed were amplitude sweeps to determine at what shear rate the paste starts to flow, and three interval thixotropy tests to determine the recovery of the pastes. In the article by Kleger et al. (2019), they mentioned wall-slip occurring during the measurements when using a flat parallel plate geometry. To decrease the risk of wall-slip in the measurements, sandpaper was glued onto disposable parallel plates. This decreased the effect of wall-slip and improved the measurement accuracy. The sandpaper coated parallel plates are shown in Figure 13 below.

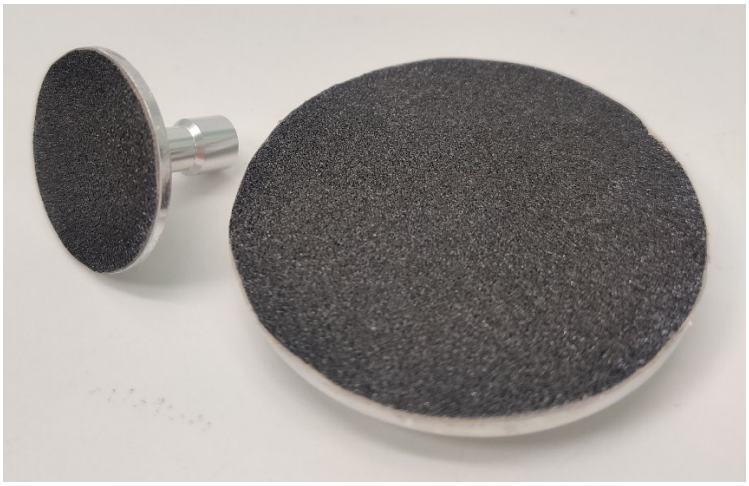

Figure 13 *Sandpaper was glued onto disposable parallel plates to reduce wall-slip and enhance measurement accuracy.*

3.2 Inorganic structures II

For the inorganic pastes, two different approaches were tested. The first approach was replacing salt with inorganic particles, and the second approach was using an alternative inert binder.

3.2.1 Chemicals

Chemicals used for the preparation of inorganic pastes were AOT, Paraffin oil, “inorganic material 1” (IO1), “inorganic material 2” (IO2), “binder A”, and “binder B”. All pastes contained either the IO1 or IO2 material together with binder B, regardless of the rest of the components in the paste.

3.2.2 Paste preparation

Preparation of AOT-containing inorganic paste

The preparation of pastes containing AOT differed slightly from the preparation of salt paste in that no particles were ball milled. Instead, AOT was dissolved in Paraffin oil by magnetic stirring overnight. The inorganic mixture of either IO1 or IO2, together with binder B, was then added to the dissolved mixture and speed mixed in a SpeedMixer to obtain a well-dispersed paste. Different ratios of the components were tested to obtain an

extrudable paste, but these prepared pastes were inconsistent and seemed to separate when sheared. Due to the inconsistency and lack of performance when printed, an alternative paste was tested.

Preparation of solids loaded pastes with binder A

A solids loaded paste with binder A was chosen as an alternative approach since it is not dependent on chemical interactions with the inorganic solids. A gel-like substance was prepared by mixing 25 wt-% of a polymer with deionized water. The binder was prepared by stirring the components overnight, allowing the polymer to disperse well in the water.

The addition of inorganic solids was done by measuring a required amount of binder A and cooling it down. The inorganic particles were added in different ratios, and the mixture was speed mixed to obtain a well-dispersed solids loaded paste. The temperature in the sample increases rapidly when speed mixed, which allowed the paste to solidify while dispersing the solids evenly throughout the paste. A homogenous printable paste with up to 75 wt-% of solids was obtained.

3.2.3 3D printing of inorganic paste

AOT-containing paste

Inorganic pastes containing AOT were printed directly on a filter paper. After completion of each structure, they were covered in graphite powder to enhance drying of the structures. Inconsistency in the extrusion of the paste required continuously increasing printing pressures to maintain an even extrusion of the paste.

Solids loaded paste with binder A

The solids loaded pastes with binder A were printed on aluminum foil. The adhesion between the paste and the aluminum foil was sufficient enough to allow the first printed layer to stick properly to the surface, while still allowing removal of dried structures without breaking them. The samples were dried at room temperature for 1-2 days, after which the structures could be removed. With binder A, the consistency in extrusion of the paste was improved.

3.2.4 Post-processing of inorganic green bodies

Post-processing of the inorganic green bodies was performed in the same oven as used for the salt structures, but with modified intervals to match the inorganic materials. As for the salt structures, a thin layer of graphite powder was placed on the platform to avoid adhesion between the structures and the platform, and to allow free contraction as the structures shrunk.

3.2.5 Rheology measurements

For the rheological measurements, 12 different pastes of varying particle-sized inorganic materials were prepared. All pastes contained 75 wt-% solids to be more easily comparable between themselves. As printing of these pastes points towards an improved extrudability with a broader particle size distribution, the pastes for the rheology measurements were prepared with a mixture of different particle sizes. The desired particle size for each paste accounted for 50% of the total amount of the specific inorganic material. As a reference sample, the alternative binder with no solids-loading was used. A parallel plate geometry with disposable plates was used for the measurements. Unlike prior measurements with the salt pastes, no sandpaper coating was necessary as there was not a similar wall-slip behavior.

3.3 Equipment

In this section the equipment used for the experimental part of the thesis are described.

PHILLIPS MiniMill

For the preparation of salt pastes, the components were ball milled to a paste with the PHILLIPS MiniMill. It can be used for high-speed grinding of either dry or wet organic or inorganic samples. The two milling cups in the instrument rotates around their own axis to create centrifugal forces in the process. The rotational speed can be adjusted between 400 – 3400 rpm.

By dry grinding samples an average particle fineness of approximately 20 µm can be obtained, while wet grinding can decrease the fineness of the particles to approximately 1 µm. By increasing the speed and the time of the grinding process, a larger quantity of fine particles can be obtained. In Figure 14 below the instrument is shown.

Figure 14 *Ball mill used for the preparation of salt pastes.*

Brinter ONE – Multitool 3D bioprinter

For the printing process a Brinter ONE Multitool 3D bioprinter was used (Brinter, 2023). The printer has a large variety of different printheads, which can easily be changed and are automatically recognized by the printer. The printer allows up to 4 different printheads in the tool sockets onboard at the same time, which can be changed automatically, allowing printing of different materials in the same construction. Depending on the printhead, the printer has optional cooling and heating functions from 4°C (min) to 250°C (max), while the temperature of the print bed can be changed between 4°C and 100°C. The pressure range of the printer is 0-6 bar, and it has a maximum print speed of 80 mm/s. The printheads are compatible with standard Luer-lock syringes (10 and 3 ml) and needles. Minimum step size in X, Y, and Z directions is 3 µm, and the maximum build volume is 304 x 174 x 80 mm. The printer is equipped with a camera for live process view, and some of the printheads are equipped with photocuring UV/visible light LEDs of 365, 405, and 450 nm.

For the experiments conducted in this thesis, a pneumatool printhead was used without heating or cooling of either the printhead or the print bed. No photocuring was necessary as the feedstock showed rapid recovery after extrusion. The structures were printed on a glass surface covered with either filter paper or aluminum foil to prevent sticking to the surface. The printer is shown in Figure 15 below.

Figure 15 *The Brinter ONE with 4 printheads onboard (Brinter, 2023).*

Phoenix Microwave Muffle furnace

For sintering and post-processing, a Phoenix Microwave Muffle Furnace was used (CEM Corporation, 2006). The maximum temperature of the furnace can either be 1000°C or 1200°C, depending on furnace system in use. The furnace at Åbo Akademi University is assumed to be a "High Capacity Furnace" with a maximum temperature of 1000°C. The volume of the sample chamber is 5.0 liters.

The furnace allows 8 steps of increasing or decreasing temperatures. For each step a dwell time can be set at desired temperatures.

Anton Paar MCR 702e MultiDrive

For the rheological measurements of the pastes, an Anton Paar MCR 702e MultiDrive modular compact rheometer was used (Anton Paar GmbH, 2023). The equipment can run different measurement modes, such as Dynamic Mechanical Analysis (DMA) in torsion, compression, tension, and bending. It is equipped with an additional lower drive unit, allowing rheological measurements with two drive units and torque transducers at once.

The rheological measurements that were conducted for this thesis were amplitude sweeps and three interval thixotropy tests. In Figure 16 below, the Anton Paar MCR 702e MultiDrive is shown.

Figure 16 *The rheometer model used for the measurements (Anton Paar GmbH, 2023).*

FlackTec SpeedMixer

A FlackTec SpeedMixer model DAC 330-100 L was used to mix pastes of the inorganic particles (FlackTec, 2022). The model has a mixing weight capacity of up to 200 g and a cup volume capacity of up to 515 ml. The instrument allows bubbleless mixing of powders, semi-solids, creams, and more. The bladeless technology uses a Dual Asymmetric Centrifuge (DAC) to rotate the cup with the sample at an angle clockwise around a central axis, while simultaneously counter rotating the cup upon its own axis. This forces the material to flow against itself, removing bubbles from the sample. The DAC technology is illustrated in Figure 17 below.

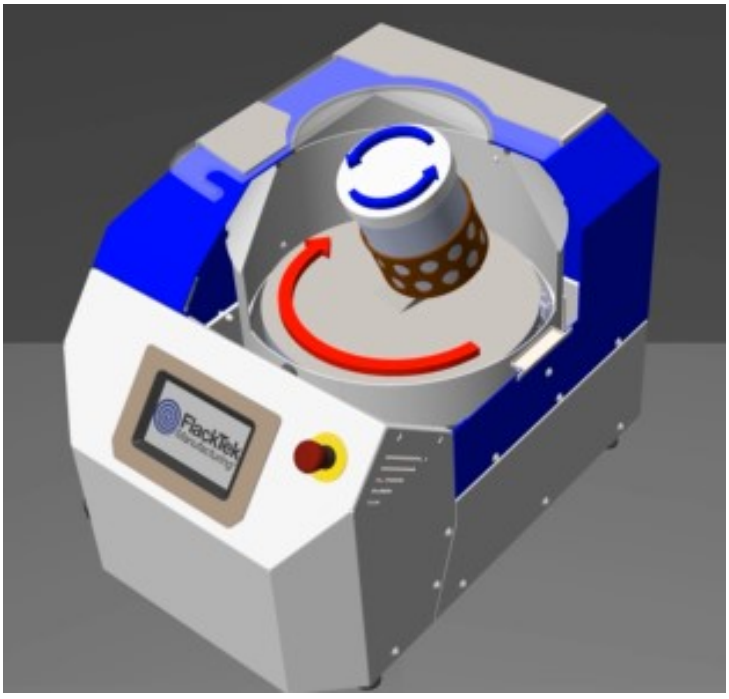

Figure 17 *Illustration of the FlackTec SpeedMixer's DAC technology (FlackTek, 2022).*

4 Results and discussion

In this chapter, the 3D printing process, and a collection of results from different measurements are presented and evaluated. Measurements and visual analyses that were done are Amplitude sweeps and 3ITT, Differential Scanning Calorimetry (DSC), Thermogravimetric Analysis (TGA), Scanning Electron Microscope (SEM), Energy Dispersive Spectroscopy (EDS), and 4-Point Bending tests.

4.1 Rheology measurements

For the evaluation of paste properties during the printing process, two different rheology measurements were performed. Amplitude sweeps were conducted to evaluate the flowability of the paste when extruded through the nozzle, while three interval thixotropy tests were conducted to evaluate the recovery of the paste after extrusion.

The amplitude sweeps were performed with a stress amplitude that increased logarithmically with a constant frequency at 1 rad s^{-1}. The 3ITT measurements were performed in three intervals, i.e., oscillation – rotation – oscillation. The oscillating intervals were done at 0.01% shear rate and 10 Hz oscillation (rest state), and the rotational interval at 100 $1s^{-1}$ shear rate. In the sections below, the results of the measurements are presented.

4.1.1 Rheology measurements of salt paste

Rheological measurements were conducted on salt pastes of different compositions and contents, but due to inaccuracy in the measurements occurring from wall-slip only a few measurements of relevance were obtained. With a flat parallel plate geometry, no measurements could be obtained. Therefore, sandpaper was glued on disposable parallel plates to obtain the data shown in Figures 18-25 below. It is worth mentioning that the obtained data is insufficient to prove how the paste behaves, but sufficient enough to make an assumption of the behavior pattern of the different salt pastes.

Two different surfactants, AOT and SDS, were tested in the pastes. Based on the article “3D Printing of Salt as a Template for Magnesium with Structured Porosity” by Kleger et al. (2019), and based on the experiments conducted on the paste, AOT was a better

choice as it allows a larger amount of NaCl in the paste than SDS. Similar results were obtained from amplitude sweeps of salt pastes containing 10 wt-% of SDS, respectively 2.5 wt-% AOT, with respect to the amount of NaCl used in the pastes. Additionally, a smaller amount of Paraffin oil was required for pastes prepared with AOT. Therefore, a greater solids loading can be achieved with AOT as surfactant.

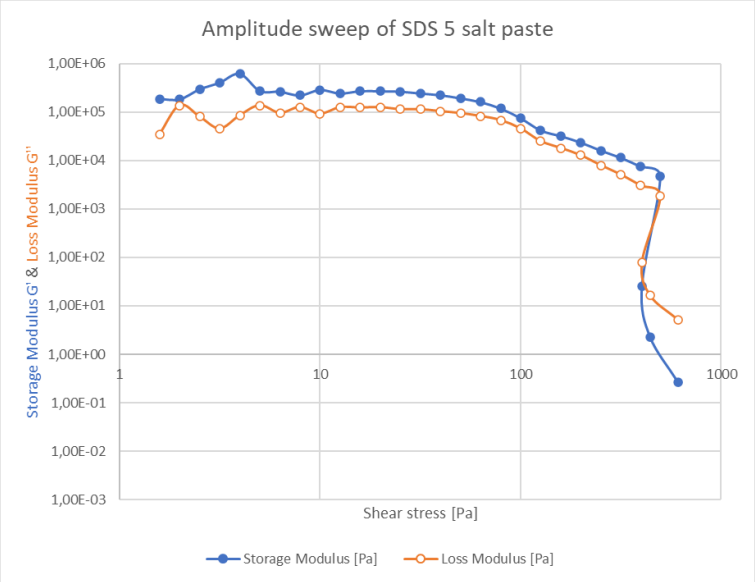

Figure 18 *Amplitude sweep of a salt paste with 5 wt-% of SDS (with respect to NaCl amount) as surfactant.*

The "SDS 5" paste in Figure 18 appears to be shear-thinning and has a crossover point at about 500 Pa shear stress. Either the structure breaks instantly when reaching a certain point of shear, or the measurement lacks accuracy. Kleger et al. (2019) reported that a 10 wt-% of SDS referred to the mass of NaCl used in the paste exceeded the absolute surfactant concentration needed to bond the paraffin oil and NaCl. Thus, 5 wt-% of SDS is insufficient to ensure homogeneity in the paste. All pastes containing SDS as surfactant were prepared with 28.6 wt-% of paraffin oil, referred to the total mass of the paste.

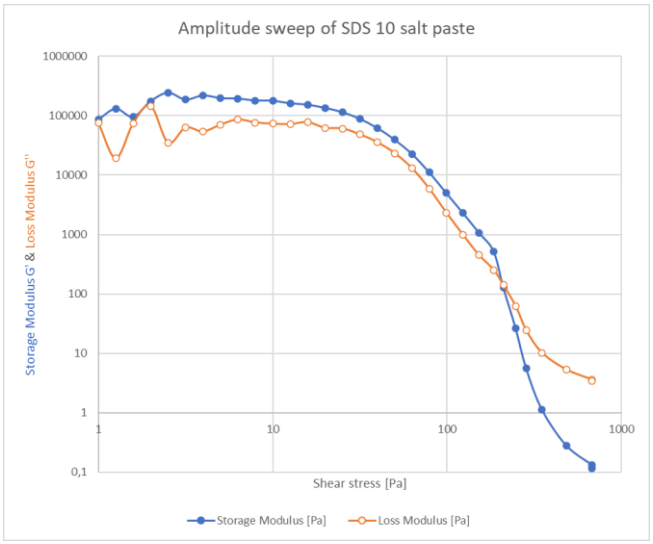

Figure 19 *Amplitude sweep of salt paste with 10 wt-% of SDS.*

With 10 wt-% of SDS referred to the total mass of NaCl used, a more accurate measurement was obtained. In Figure 19, the paste shows a shear-thinning behavior and a crossover point at about 210 Pa shear stress. As mentioned above, the absolute surfactant concentration is much lower for AOT than for SDS. Initial pastes containing AOT were prepared similarly to the ones with SDS, having 28.6 wt-% of paraffin oil. As seen below in Figure 20, AOT-containing pastes requires less paraffin oil to behave similarly to the salt paste with 10 wt-% of SDS, allowing a greater amount of NaCl.

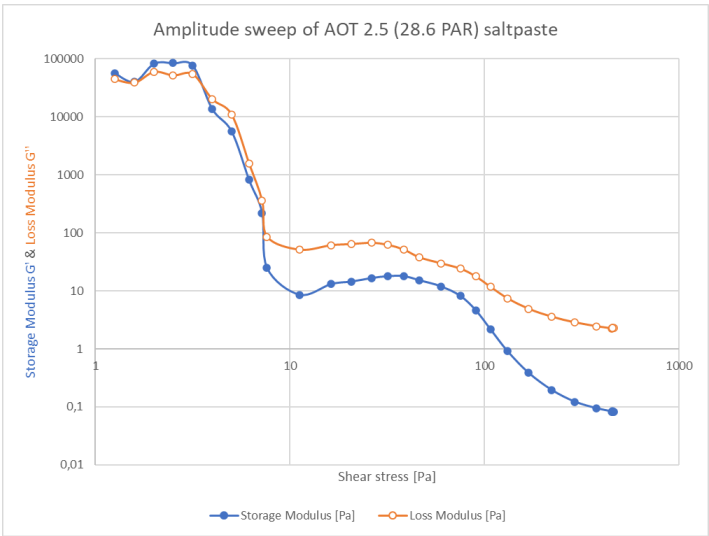

Figure 20 *Amplitude sweep of salt paste with 2.5 wt-% of AOT (NaCl) and 28.6 wt-% of paraffin oil (total mass).*

With 28.6 wt-% of paraffin oil, the AOT-containing paste was liquid-like and had poor shape retention. The liquid-like behavior can also be seen in Figure 20 above, where G' is greater than G'', but only at low shear stresses as the crossover point occurs already at a shear stress beneath 10 Pa. To compensate the lack of shape retention, pastes with a decreased amount of paraffin oil were prepared.

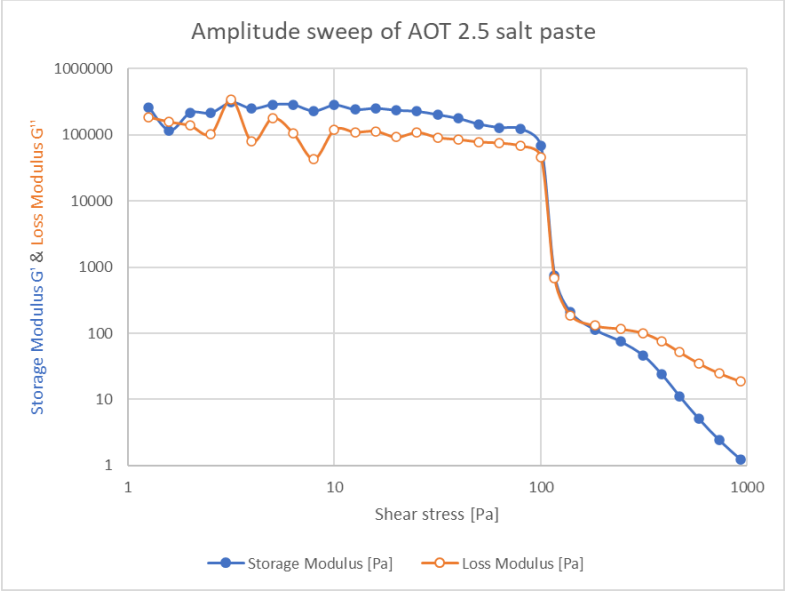

Figure 21 *Amplitude sweep of salt paste with 2.5 wt-% of AOT (NaCl) and 20 wt-% of paraffin oil (total mass).*

As seen in Figure 21, by decreasing the amount of paraffin oil in the AOT-containing pastes, a similar shear-thinning behavior occurred as for the pastes with 10 wt-% of SDS, referred to amount of NaCl used. A shear-thinning paste with a crossover point at a shear stress just above 100 Pa was obtained with proper shape retention. Further evaluation of the paste contained changes in the AOT content and finding maximum and minimum NaCl content in the paste while maintaining printability. For the evaluation of the minimum salt content paste, the main criteria was that the structure maintained its shape after extrusion, while the criteria for the maximum salt content paste was that it remained extrudable.

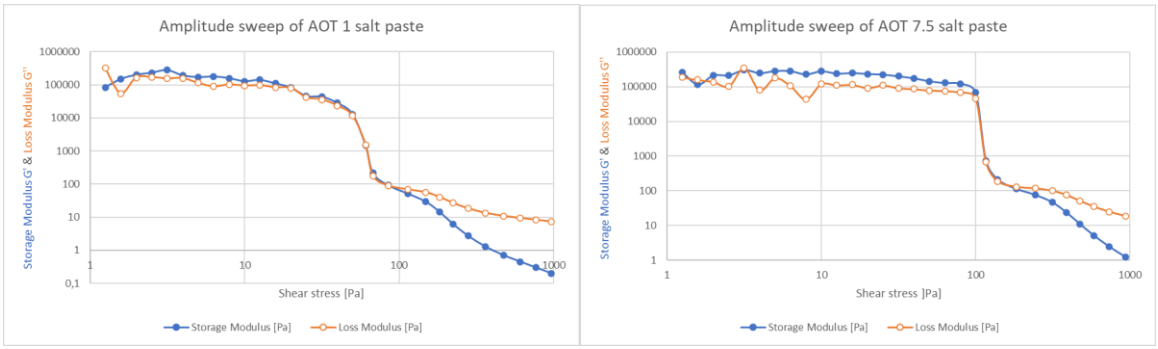

Figure 22 *Left: Amplitude sweep of salt paste with a decrease in AOT content (1 wt-% of amount NaCl). Right: Amplitude sweep of salt paste with an increase in AOT content (7.5 wt-% of amount NaCl).*

Figure 22 above show the effect of changes in AOT content in salt pastes with 20 wt-% of paraffin oil. If the content is decreased, the amount of surfactant is insufficient to bond the oil and NaCl to achieve a fully homogenous paste. If the content is increased above the absolute surfactant concentration, no apparent changes occur in the rheology of the paste as the results are almost identical with the ones obtained from the 2.5 wt-% of AOT-containing paste. It can be concluded that the optimum amount of the surfactant AOT used in the paste is approximately 2.5 wt-%, referred to the amount of NaCl present in the paste, when the amount of paraffin oil is 20 wt-% of the total mass.

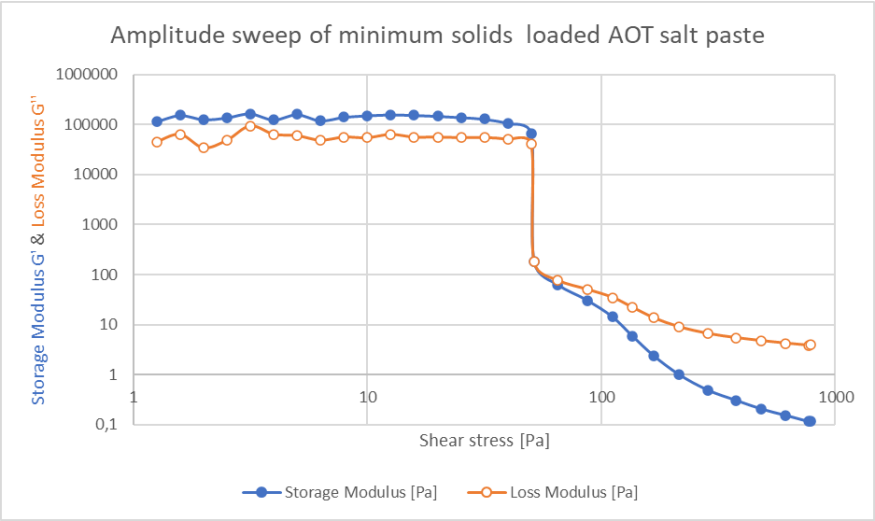

Figure 23 *Amplitude sweep of minimum solids loaded salt paste with 2.5 wt-% AOT.*

The minimum solids loaded salt paste with 2.5 wt-% of AOT, referred to amount of NaCl, is mainly an indicative assumption of how low the content of Paraffin oil can be while maintaining the structures shape after extrusion. This paste in Figure 23 contained 73.13 wt-% NaCl and 25 wt-% paraffin oil. For small "button" structures with a diameter of 12 mm and a height of 3 mm, the paste had enough shape retention to maintain its shape without major deformation. Around shear stresses of 50 Pa, the crossover point where G'' > G' occurred.

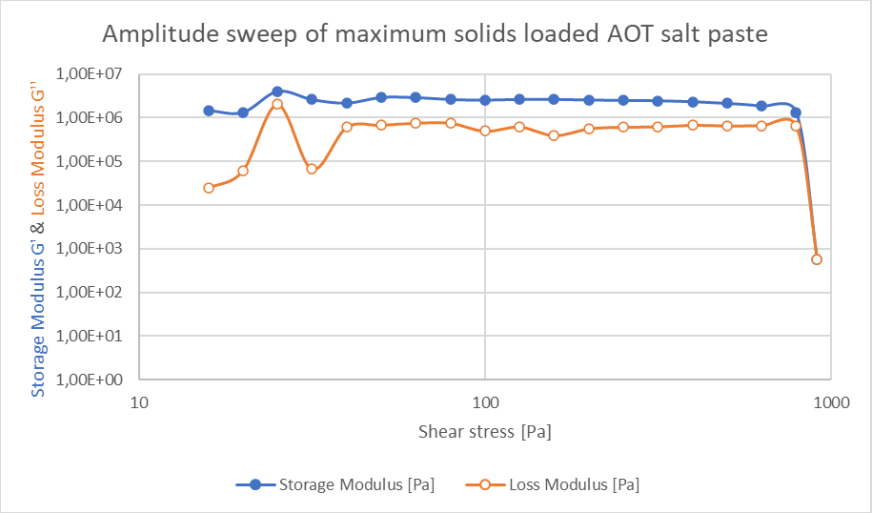

Figure 24 *Amplitude sweep of maximum solids loaded salt paste with 2.5 wt-% AOT.*

At low shear stresses no relevant points could be measured for the maximum solids loaded AOT-containing salt paste, as seen in Figure 24. Above 40 Pa, accurate measurement points occurred. Although the measuring interval was a bit too narrow, a crossover point occurred at shear stresses around 900 Pa. The limiting factor for how much NaCl could be loaded into the paste was the criteria that it needed to be extrudable with the printer. In this case, a nozzle of 0.25 mm was used and identical "buttons" as for the minimum NaCl loaded paste were printed at high pressure and low printing speed. The paste contained 82.88 wt-% NaCl, which for the small nozzle was fairly close to the maximum amount of solids that could still be extruded. By increasing the nozzle size, decreasing the printing speed, and increasing the printing pressure, a slightly higher solids content could be achieved.

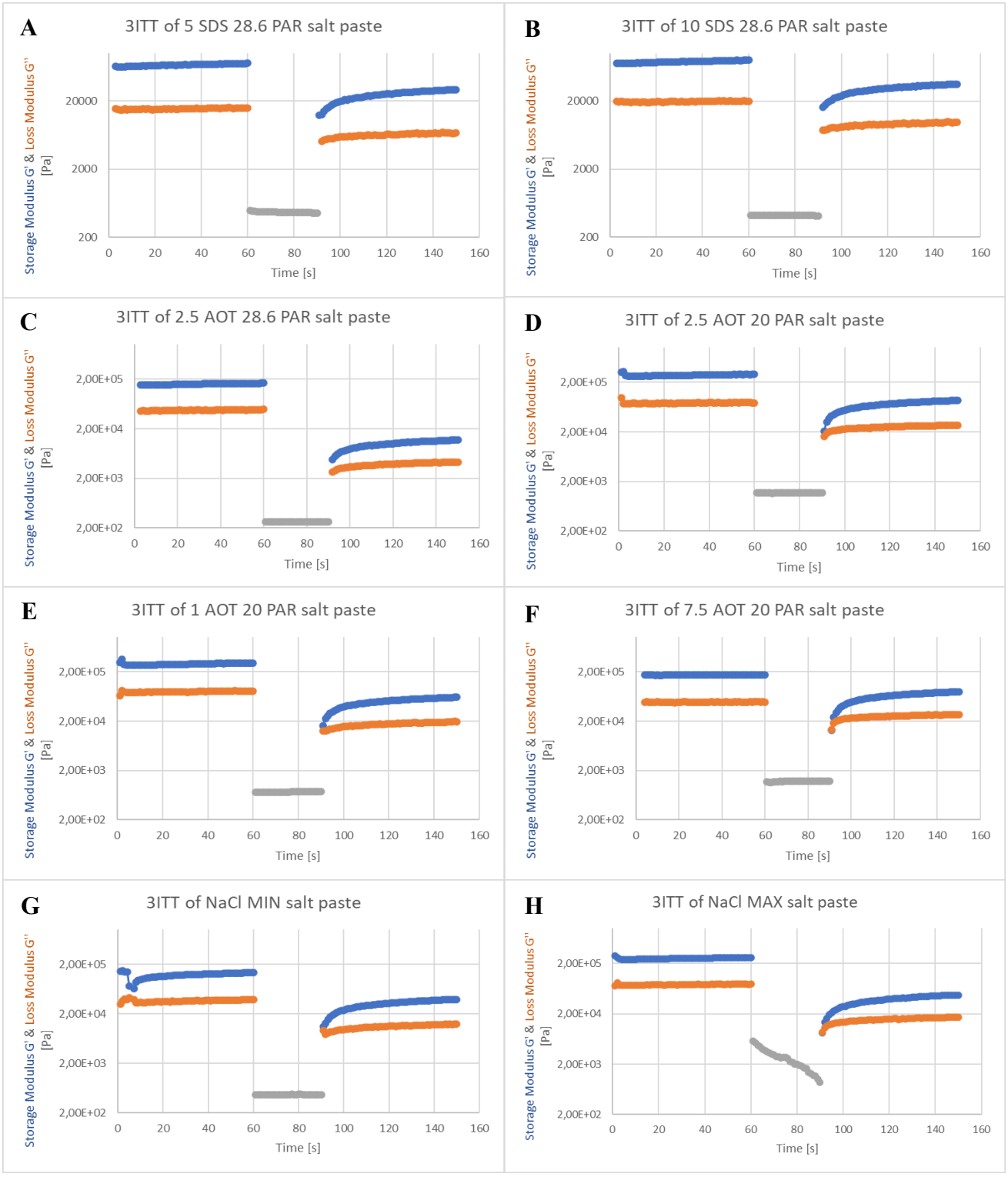

Figure 25 *Three Interval Thixotropy Test of different salt pastes. The two measurements on top, A and B, were done on pastes containing SDS, the rest of the measurements, C – H, were done on pastes containing AOT.*

The 3ITT measurement in Figure 25 shows a rapid recovery for each paste, regardless of surfactant or composition of contents in each paste. Pastes containing SDS (Figure 25 A & B) has a bit lower storage and loss modulus than those containing AOT. Apart from that, all the measurements are quite similar. The recovery from a more liquid-like structure to a solid-like structure happens within a second for every paste. To fully recover, it requires a longer time than the third recovery interval, which is 60 seconds.

The 3ITT for the paste with 28.6 wt-% paraffin oil and 2.5 wt-% AOT (Figure 25 C), referred to the total amount of NaCl in the paste, seems to have the longest recovery time to reach complete recovery. This paste was also the most liquid-like with poor shape retention. It is possible that the amount of AOT present in this paste is insufficient to bind the components into a completely homogenous paste. From this it can be deduced that pastes with optimal ratios of components will behave the same, while a paste without optimal ratios of components will lack in performance.

4.1.2 Rheology measurements of inorganic paste

For the rheological measurements of inorganic pastes, 12 similar pastes with solids loadings of 75 wt-% were prepared. The differences in the pastes were different particle sizes and content of each particle size. Not every paste that was prepared for the measurements is printable, which is proven by the results of the measurements, hence the decision of preparing pastes with identical solids loadings was based on obtaining comparable results where the effect of using different sized particles can be seen.

Particle sizes used for the measurements ranges from the smallest, 1000, to the largest ,80, with 600, 400, 280, 150, and 100 between them. 1000, 600, and 400 are all such fine particles that they appear as a fine powder, while larger particles can be seen with the eye. Although the content of different particles for each paste was different, they all followed the same pattern where the desired particle size, the largest of the ones used in each paste, stood for 50% of the total content of particles. Only two of the pastes were prepared with only one particle size, 1000, while the rest contained an even mixture of particles smaller than the desired size. Measurements on the two pastes containing solely the smallest particle size 1000 were unsuccessful as the pastes were too thick to measure. With a distribution of different sized particles, the flowability of the pastes were improved and

results could be obtained. Below in Figures 26-28 the results of the successful amplitude sweeps are presented alongside a reference measurement of binder A. In “Appendix A”, chapter 8, each measurement is individually presented with both the amplitude sweep and the thixotropy test and an approximated particle size distribution chart.

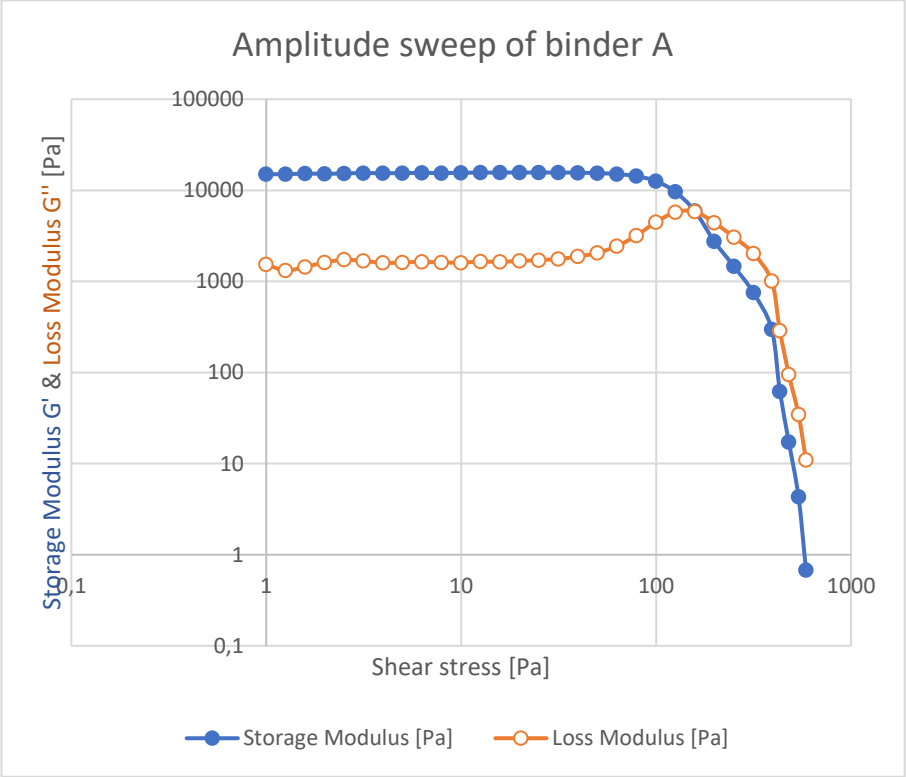

Figure 26 *Amplitude sweep of the binder A as reference sample.*

The binder A in Figure 26 shows a shear-thinning behavior and has a crossover point where the substance becomes liquid-like (G’’ > G’) at a shear stress of approximately 160 Pa.

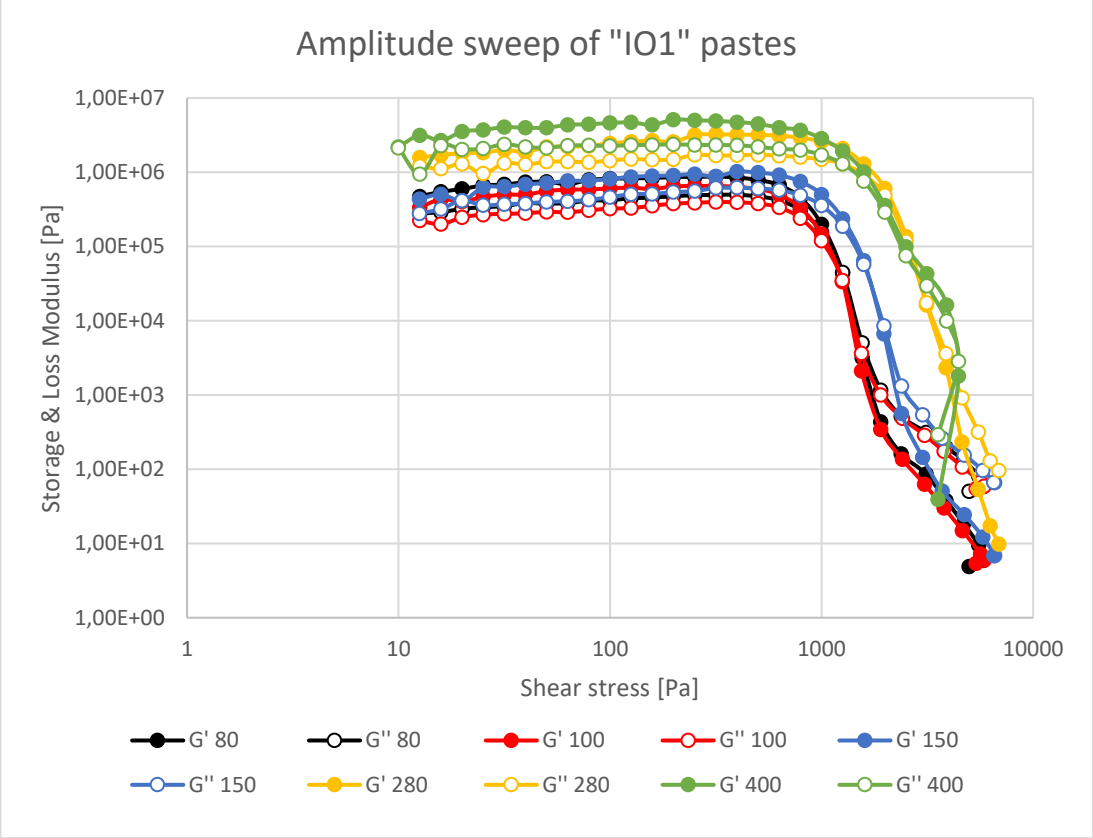

Figure 27 *Amplitude sweeps of 5 different pastes containing the "Inorganic 1" material.*

As can be seen in Figure 27 above, each paste shows a shear-thinning behavior and a crossover point where G'' > G' at shear stresses between approximately 1200-3000 Pa. The paste containing solely the smallest particles 1000 was not measurable with solids loadings of 75 wt-%, regardless of the inorganic material used (IO1 or IO2). With increased particle sizes, thus a larger size distribution of different particles, the flowability of the pastes is improved and the paste flows at lower shear stresses. Therefore, it can be concluded that a broader particle size distribution allows a greater amount of solids to be incorporated in the paste, while maintaining printability. Compared to the reference sample of binder A in Figure 26, the pastes containing inorganic materials requires much higher shear stresses to become liquid-like and flow (Figures 27 & 28). From the amplitude sweep graph of IO1 400, the last two measurement points are removed as they appeared to be irrelevant. These points are present in "Appendix A" in chapter 8.

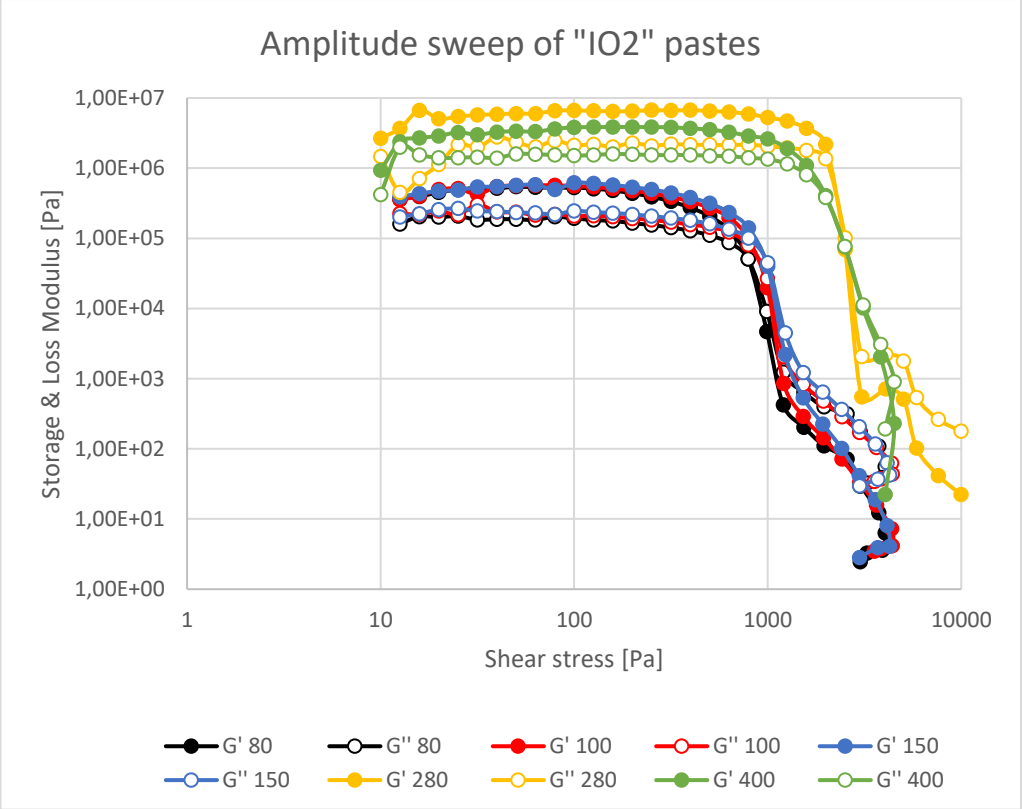

Figure 28 *Amplitude sweeps of 5 different pastes containing the "Inorganic 2" material.*

The amplitude sweep results of pastes containing the IO2 material (Figure 28) were quite similar to the results of pastes containing the IO1 material (Figure 27). Pastes with smaller particles and a narrower particle size distribution requires higher shear stresses to flow, while pastes with larger particles and a broader particle size distribution flow at lower shear stresses. The last two measurement points were also removed from the IO2 400 graph as they appeared to be irrelevant, like the IO1 400 graph. These points are present in "Appendix A", chapter 8.

All the measurements were quite similar regardless of inorganic material incorporated in the paste. The biggest difference appears between the IO1 280 (Figure 27) and IO2 280 (Figure 28) measurements, where the latter seemingly behaves differently after the crossover point (G'' > G'). This measurement had to be done twice, which could have affected the measurement as the paste was exposed to the atmosphere for a longer time, allowing the paste to dry more. Additionally, the pastes containing IO2 did not require as high shear stresses to become liquid-like compared to the ones containing IO1.

4.2 3D printing and post-processing of salt and inorganic structures

In this section of the chapter, both unsuccessful and successful 3D printing trials are discussed.

4.2.1 3D printing and post-processing of salt pastes

Salt structures were successfully printed after optimizing the paste preparation to enhance printability without nozzle cloggage. Depending on the content of the paste, the printing parameters had to be changed to match the paste in question. A larger amount of solids required higher printing pressure and lower printing speed, while a paste with a lower amount of solids was easier to extrude at lower pressures, allowing faster printing speed.

Salt structures were printed on different surfaces to evaluate the best possible way of handling the green bodies after completion of the printing process. Structures were printed on petri dishes, on glass surfaces, and directly on filter paper. Structures that were printed either on a petri dish or on a glass surface had to be moved to dry after completion of the printing. Since these structures were very soft, they could not be moved without freezing them using liquid nitrogen. The challenge with freezing the structures was that they more often shattered or cracked than stayed intact. The few pieces that survived the freezing process might have cracked within the structure, which could not be observed. Therefore, the most promising method was printing directly on a filter paper, which immediately starts to absorb the Paraffin oil from the structure. A shattered salt structure is shown in Figure 29 below.

Figure 29 *Salt structures shattered when attempted to freeze them with liquid nitrogen.*

The structures that were printed directly on a filter paper began to dry immediately when extruded. The drying was then further enhanced by covering the structures with graphite powder prior to the sintering process. By testing different sintering methods, it was found that the best way to obtain crack-free structures was to apply a thin layer of graphite powder on a heat-resistant platform and placing the printed green bodies on top of it to allow free contraction as the structures began to shrink. The graphite powder decomposed during the sintering process, thus left no residue on the post-processed structures.

4.2.2 3D printing and post-processing of inorganic pastes

The initial attempt to replace salt with inorganic particles was unsuccessful as separation seemed to occur in the paste. At the beginning of each print, suitable parameters could be found regarding layer height, printing pressure, and printing speed, but as the process progressed, a continuous increase of pressure was required to maintain a similar extrusion as to the preset parameters. The longer the process proceeded, the more the pressure had to be increased until the maximum pressure of 6000 mbar was reached. At this point, the paste within the syringe was too solid to be extrudable, which suggests that the oil separated from the paste. In Figure 30 below are two bars printed with the AOT-containing paste where this behavior can be seen.

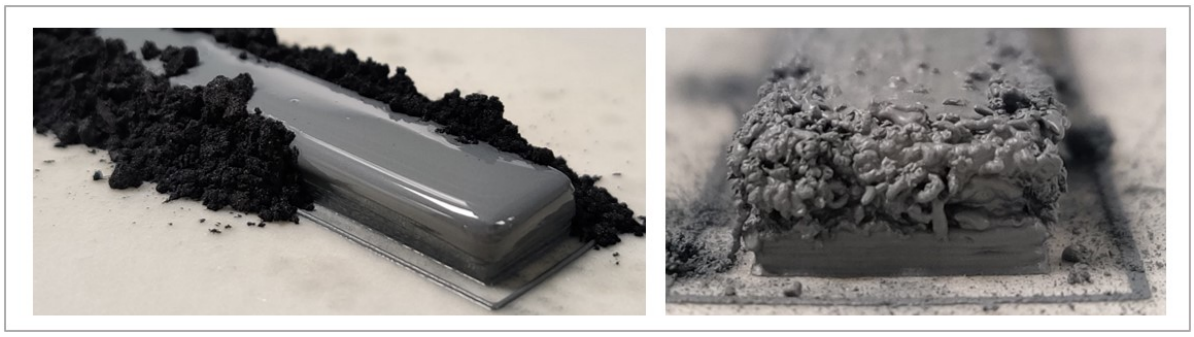

Figure 30 *The assumed separation behavior in AOT-containing inorganic pastes. The first bar of the same batch (left) seemingly contained a larger concentration of oil than the second bar (right).*

The two bars above in Figure 30 were printed with the same paste batch. The first bar seemingly contained a much larger concentration of paraffin oil than the second bar, which indicates that the lack of interactions within the paste resulted in inconsistent extrusion. The latter structure that was printed seems to have a much larger concentration of solid particles as the extrusion became uneven and required elevated pressures to be extruded. Several attempts were conducted with varying component ratios in the pastes, but the same behavior occurred.

As with the printing of salt paste, the structures of AOT-containing inorganic pastes were printed directly on a filter paper to enhance drying of the structures. However, the lack of consistency during printing with these pastes led to the decision to investigate alternative approaches. The most promising approach, given the problem of chemical interaction with the AOT, was to prepare an inert printable paste with the capability of being loaded with inorganic materials.

By replacing the Paraffin oil and the AOT with binder A, the paste immediately showed improvements in printability. The paste was consistent throughout the printing process and showed no signs of separation within the paste. Binder A was an inert gel-like substance, and different inorganic materials could be mixed into the paste without any signs of failure. A solids-loading of approximately 75 wt-% was achieved, and the paste was printable with a 1.51 mm nozzle at printing pressures around 4000 mbar, leaving enough space for pressure adjustments during the printing process. The structures were printed with a layer height of either 0.86 mm or 0.9 mm depending on the design, and the infill of the structures were done entirely of shells. Different available infill options on the 3D printer were tested but had a tendency of leaving gaps between the extruded lines. With shells as infill and a smaller nozzle size as provided information to the printer than the actual size used, these gaps could partially be avoided, almost completely filling the structures. By entering a smaller nozzle size in the software, the spacing between the extruded shells decreases, resulting in slight overlapping of the extruded shells and proper infill. To compensate printing errors in the beginning and at the end of each extruded shell, an overlap of 5% was applied in the printer’s software.

Printing directly on a filter paper was not possible with the solids loaded paste with binder A as the paper started to wrinkle. When attempting to print directly on a glass base, the

structures stuck to the glass and were not possible to remove without breaking the structures. As a solution, printing directly on a piece of aluminum foil provided enough adhesion for the first layer of printing to stick to the base, while still allowing the removal of dry structures without breaking them. Approximately 1-2 days after printing, the structures had dried to a point where they could be removed from the aluminum foil for post-processing. In Figure 31, a printed structure with the binder A containing 70 wt-% of solids can be seen.

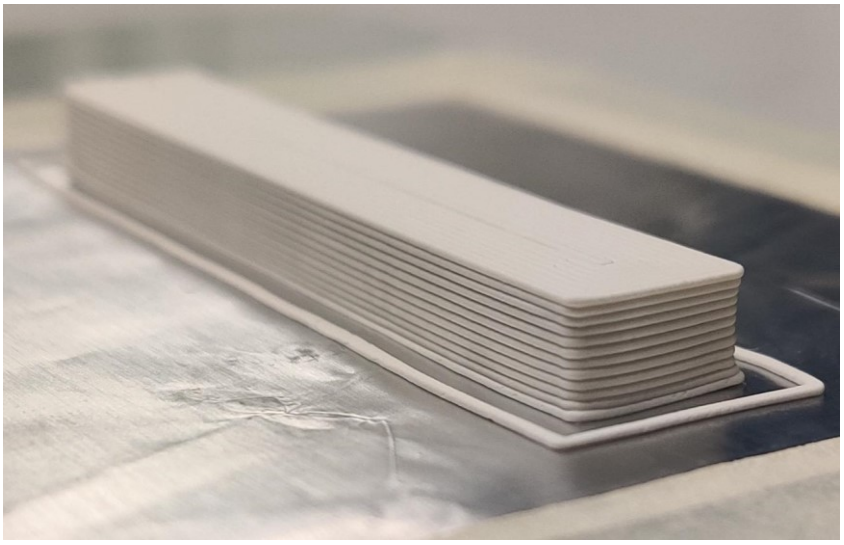

Figure 31 *One of the first printed structures with the solids-loaded binder A. Printed with a 0.33 mm nozzle at 5450 mbar pressure. With an increase in nozzle size, the paste can be extruded at lower pressures, allowing for greater amounts of solids in the paste.*

With increasing particle sizes, the printing process became more difficult as the extrusion became more uneven. By broadening the particle size distribution with addition of smaller particles, an even extrusion was obtained. The inorganic pastes were prepared with a 50% ratio of the desired particle size, while smaller sizes were added in even ratios. For instance, a paste prepared with 5 different particle sizes contained 50% of the largest particles, while the rest of the sizes each contributed with 12.5% of the total amount of the inorganic material. It was found that the extrusion was enhanced for each paste when a broader distribution of particle sizes was applied, minimizing the need for pressure adjustments during the printing process.

The printed structures dried at room temperature and were handleable after 1-2 days. For the post-process, graphite powder was used to prevent the structures from sticking to the platform and to allow free contraction as the structures shrunk.

4.3 Differential Scanning Calorimetry & Thermogravimetric Analysis

Simultaneous DSC-TGA analysis was performed on salt pastes, green bodies, and sintered structures. The samples were placed in a 90 µl alumina sample cup. The pastes were adjusted to roughly cover the bottom of the sample cups, while small pieces of the solid samples of green bodies and sintered structures were cut and placed in the sample cups. The solid samples weighted around 15-17 mg each. The measurements were performed under synthetic air, a 50/50 mixture of N_2 and O_2, and with a flow rate set to 100 ml/min. The measurement temperature was set to ramp from 30-700 °C with an increase of 20 °C/min.

For the evaluated salt pastes, three different measurements at different stages of the process were conducted. These stages were done on samples prior to printing, after printing, and on sintered structures. In Figure 32 below, a graph from the DSC analysis on pastes, green bodies, and sintered structures containing either SDS or AOT as surfactant is shown.

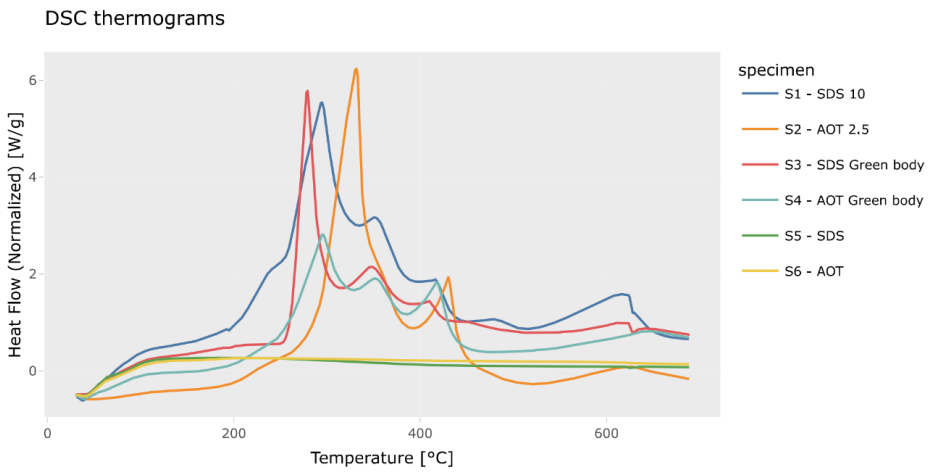

Figure 32 *DSC on salt pastes, green bodies, and sintered structures containing either SDS or AOT as surfactant. S1 & S2 are paste specimens, S3 & S4 are green body specimens, and S5 & S6 are sintered structures.*

In Figure 32, S1 and S2 are the paste specimens, S3 and S4 are the green body specimens, and S5 and S6 are the sintered structures. According to the studies on the thermal behavior of pure SDS and pure AOT performed by Kleger et al. (2019), SDS starts to degrade at approximately 170°C, and AOT at approximately 193°C. Their evaluation of the thermal behavior of pure paraffin oil reveals that the oil starts decomposing at approximately 140°C and is almost completely decomposed around 360°C. An interesting change in thermal behavior was reported for a paste prepared of NaCl, paraffin oil, and AOT, where the thermal degradation of AOT shifted towards higher temperatures compared to the obtained data from the measurements on pure AOT. When present in the paste, the thermal degradation of AOT began at approximately 363°C, which is 170°C higher than of pure AOT. This finding was reported as an energetically favorable absorption of surfactants to the surface of the NaCl particles.

Based on the findings of changes is thermal behavior of surfactants present in a paste, it can be concluded that the highest peaks in the DSC graphs indicates the decomposition of paraffin oil in the pastes or green bodies. The peaks at elevated temperatures indicate the decomposition of the surfactant present in the paste. The TGA analysis performed on the same samples proves these results as the decreases in wt-% is greater in the beginning of the slope, after which it decreases less until both the paraffin oil and present surfactant has decomposed completely. Figure 33 shows a graph of the TGA analysis on the same samples of pastes, green bodies, and sintered structures.

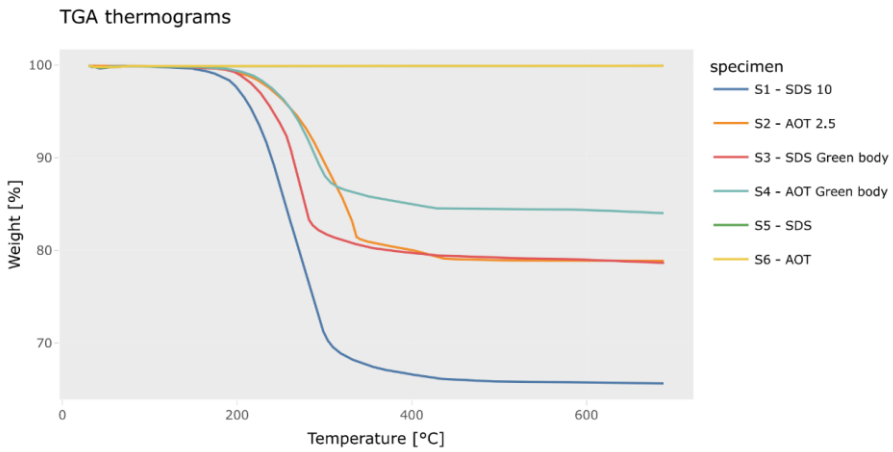

Figure 33 *TGA on salt pastes, green bodies, and sintered structures containing either SDS or AOT as surfactant. The S5 and S6 lines are parallel and thus cannot be seen separately.*

The results from the TGA analysis are as expected. A clear decrease in wt-% is seen for the two pastes S1 and S2, while a smaller decrease is seen for the green bodies S3 and S4. The smaller decrease of wt-% in the green bodies is due to prior removal of paraffin oil by covering the printed structures in graphite powder before running the measurement. The sintered structures, S5 and S6, does not decrease in wt-% as they only contain sintered NaCl. Any decreases for these specimens would indicate the presence of impurities in the sample cups.

Based on the discoveries by Kleger et al. (2019) about the elevated decomposition temperature of surfactants in a paste, and the greater amount of paraffin oil compared to surfactant present in the paste, the steeper and greater decrease in wt-% indicates the decomposition of paraffin oil. The steepness of the slope decreases at temperatures above 300°C, at which the surfactants start to decompose.

Based on the results obtained from the TGA analysis, SDS seems to decompose at lower temperatures than AOT. However, the same behavior can be observed where the decomposition temperature of SDS occurs at an elevated temperature when present in a NaCl-containing paste, compared to the decomposition temperature for pure SDS, which occurs around 170°C. Therefore, the same energetically favorable absorption occurs in both AOT and SDS-containing pastes.

After the removal of paraffin oil and surfactants, the specimens reach an equilibrium where no apparent decreases in wt-% can be observed. Any residual paraffin oil or surfactant that could still be present would disappear at these elevated temperatures. A minimal decrease in wt-% can be observed for the pastes and green bodies towards the end of the measurement. This occurs as the temperature at the end of the measurement is close to the sintering temperature of NaCl, which is around 690°C.

4.4 Scanning Electron Microscope & Energy Dispersive Spectroscopy

Scanning Electron Microscope and Energy Dispersive Spectroscopy measurements were conducted to obtain information about the surface and content of the post-processed structures.

4.4.1 SEM-EDS of salt structures

SEM-EDS revealed the formation of Na_2SO_4 between the salt grains of the salt structures after the sintering process. This was expected as it was reported by Kleger et al. (2019) in their research. The SEM images below in Figures 34-37 shows the surface of sintered salt structures containing SDS or AOT as surfactant at different magnifications.

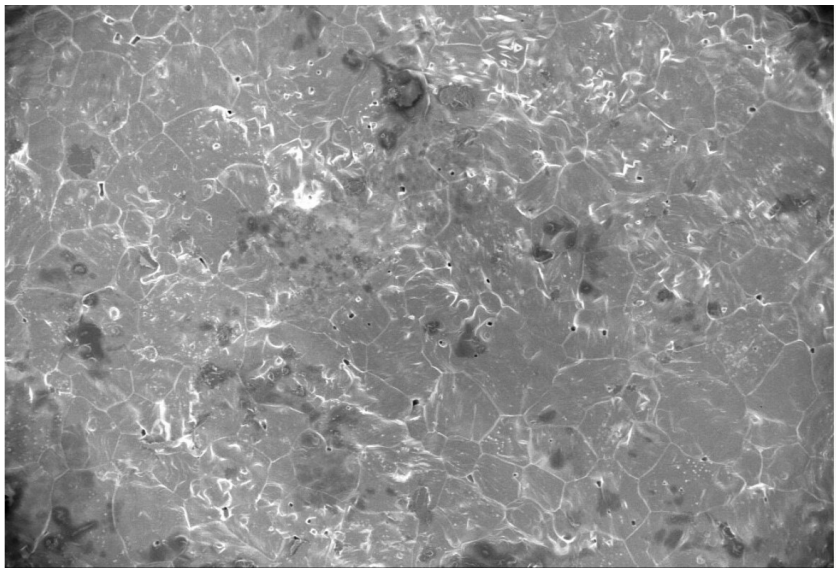

Figure 34 *SEM of sintered AOT-containing salt structure with a magnification of 102X.*

In Figure 34 above, the surface of a sintered salt structure containing AOT as surfactant is seen. With a relatively low magnification, the merged salt grains occurring in the sintering process can be observed. Small pores are also present on the surface which could have appeared as trapped air within the structure emerges to the surface during the sintering process. At this magnification, no Na_2SO_4 can be seen.

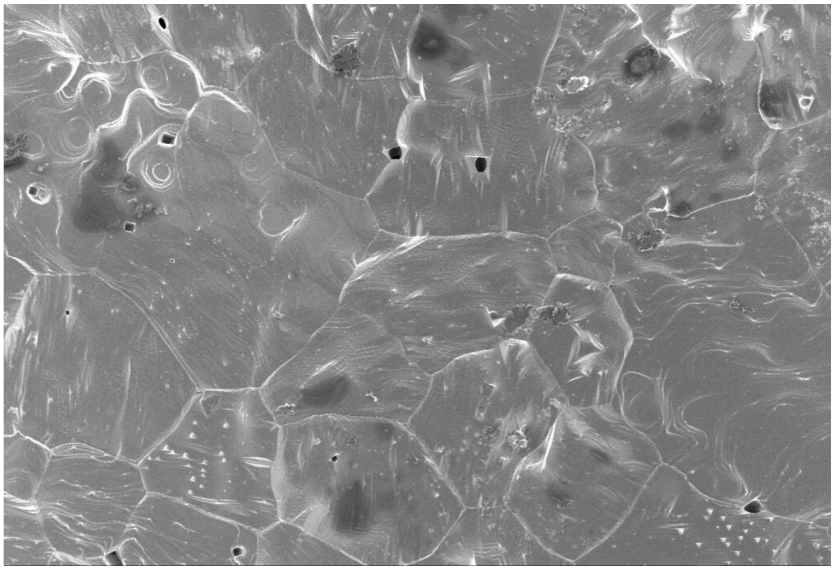

Figure 35 *SEM of sintered AOT-containing salt structure with a magnification of 280X.*

As the magnification increases, it became clearer how densely packed the salt grains are after post-treatment (Figure 35). Although the NaCl was ball milled for the paste preparation, a great variety of grain sizes can be seen. At this magnification formations of Na_2SO_4 starts to appear in the interface between salt grains. However, additional magnification is required for theses formations to appear clearly.

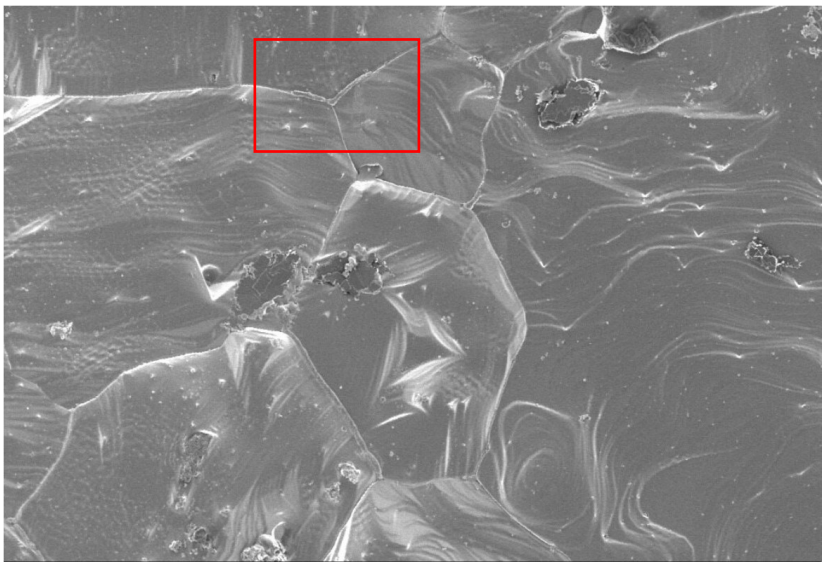

Figure 36 *SEM of sintered AOT-containing salt structure with a magnification of 636X.*

In Figure 36, the formation of Na_2SO_4 can be observed as thick lines at the interface of the grains. Highlighted in the image, one of these formations can be seen. By further increasing the magnification, the formation appears clearly, as seen in Figure 37.

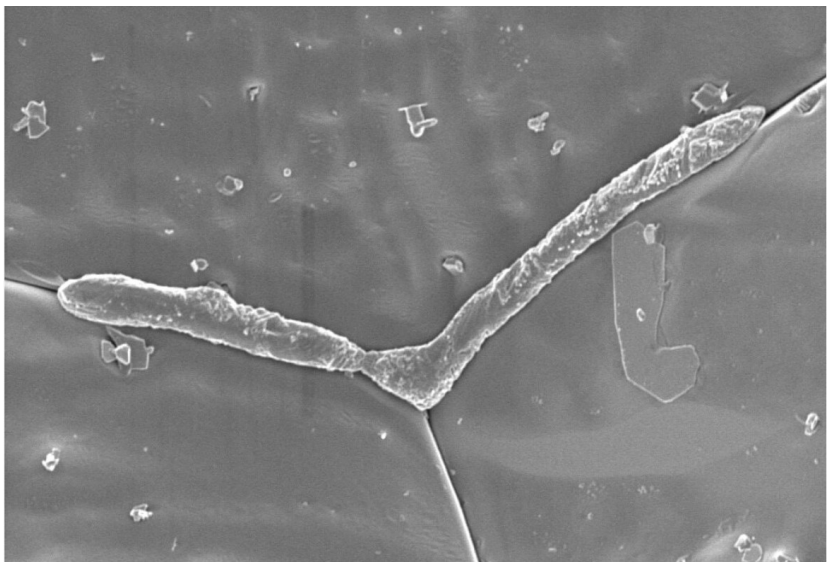

Figure 37 *SEM of sintered AOT-containing salt structure with a magnification of 5580X. A Na_2SO_4 formation appears at the interface of salt grains.*

In Figure 37, a small formation of Na_2SO_4 located at the interface of salt grains can be seen. Kleger et al. (2019) calculated a theoretical value that 0.246 g of Na_2SO_4 is formed from 1 g of SDS, and 0.15975 g from 1 g of AOT. Therefore, the amount of Na_2SO_4 formed is much lower for salt pastes with AOT as surfactant. By evaluating a formation site with an EDS analysis, the content of an interface formation can be obtained. Below in Figure 38, an EDS image of a Na_2SO_4 formation is shown.

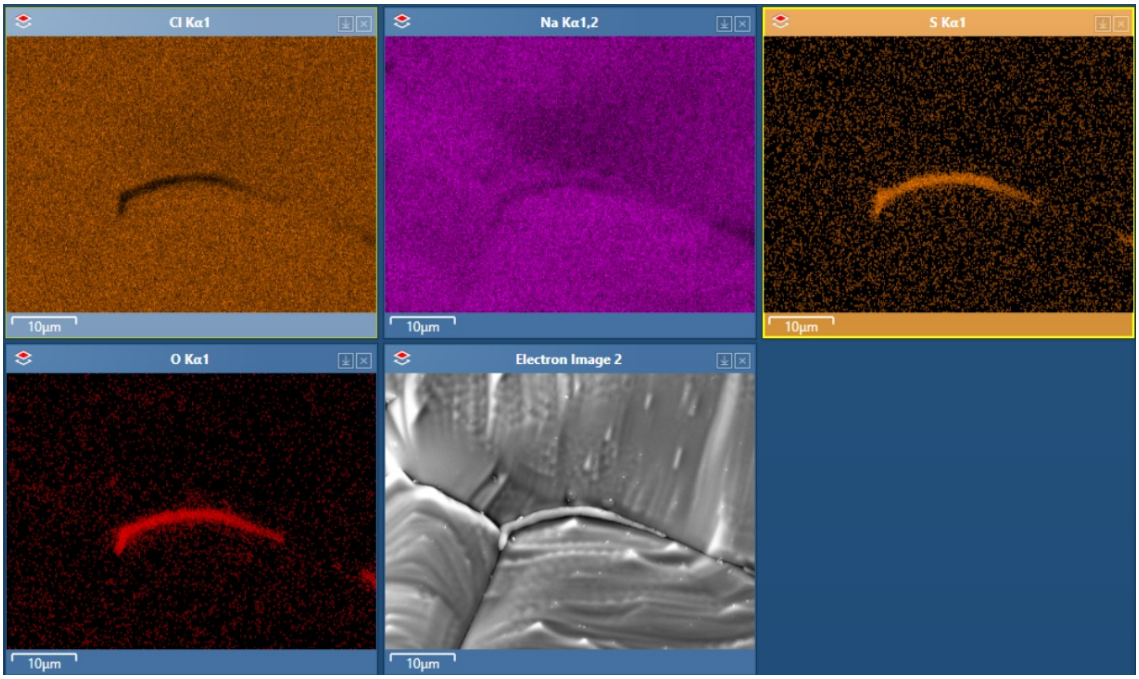

Figure 38 *EDS image of a Na_2SO_4 formation site.*

In the images of Figure 38, the presence of chloride, sodium, sulfur, and oxygen is presented as colors at their respective appearing sites. The salt grains consisting of chloride and sodium covers most of the area, except for the formation at the interface of the grains. This formation consists of sodium, sulfur, and oxygen, indicating the formation of Na_2SO_4 at the site. There is a clear blank spot at the formation site in the image where chloride appears. In Figure 39 below the amount of chloride, sodium, sulfur, and oxygen present in the EDS image is presented in weight percentage.

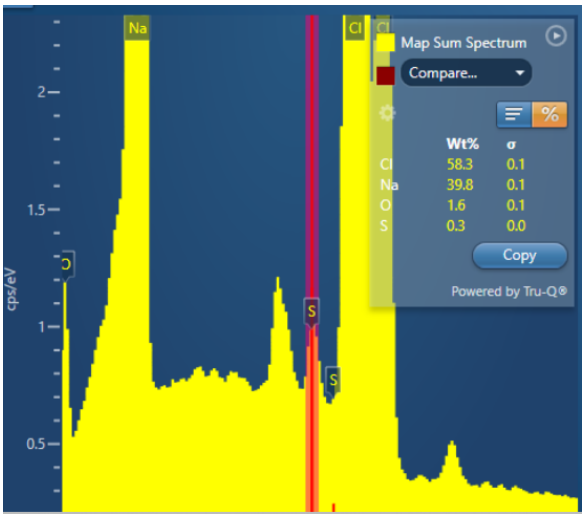

Figure 39 *Amount of each component present in the EDS image in Figure 38 presented in weight percentages.*

In Figure 40 below, crosscut SEM images of a sintered salt structure containing AOT reveals the dense nature of the structure at 37X and 197X magnifications.

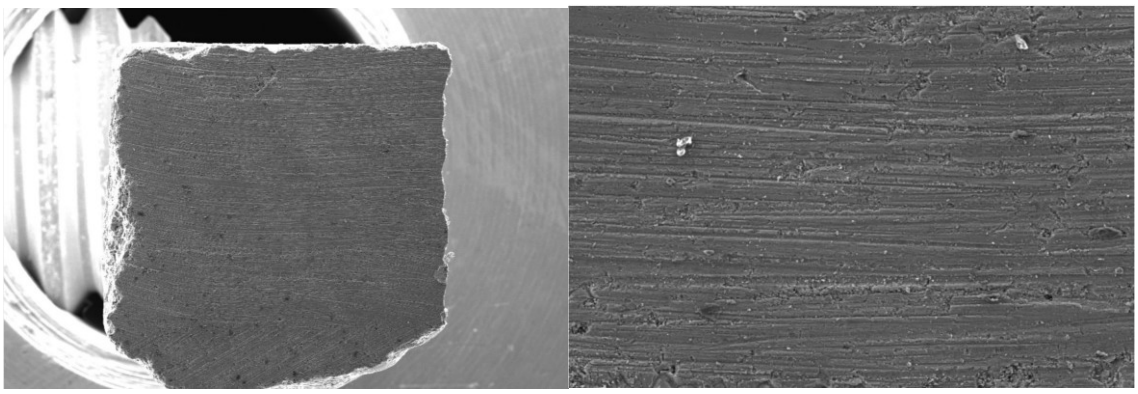

Figure 40 *Crosscut SEM images of a AOT-containing salt structure. Left: 37X magnification. Right: 197X magnification.*

No apparent air channels from the printing process can be seen in the crosscut SEM images above (Figure 40). At the crosscut the structure seems filled and dense. However, it must be taken into consideration that the surface may have deformed as the structure was cut, which can be seen on the image to the right as scratches on the surface.

In Figure 41 below, a collection of SEM images at different magnifications of a salt structure containing SDS as surfactant is presented. As the AOT-containing pastes were considered favorable with the capacity of a higher solids loading due to the less required surfactant amount, and a less required amount of paraffin oil, less evaluations on the SDS-containing pastes were performed. This applies to most measurements and evaluations performed on the salt structures as it occurred at an early stage in the project that the AOT-containing pastes performs better. Thus, no EDS images were taken on the salt structures with SDS as surfactant.

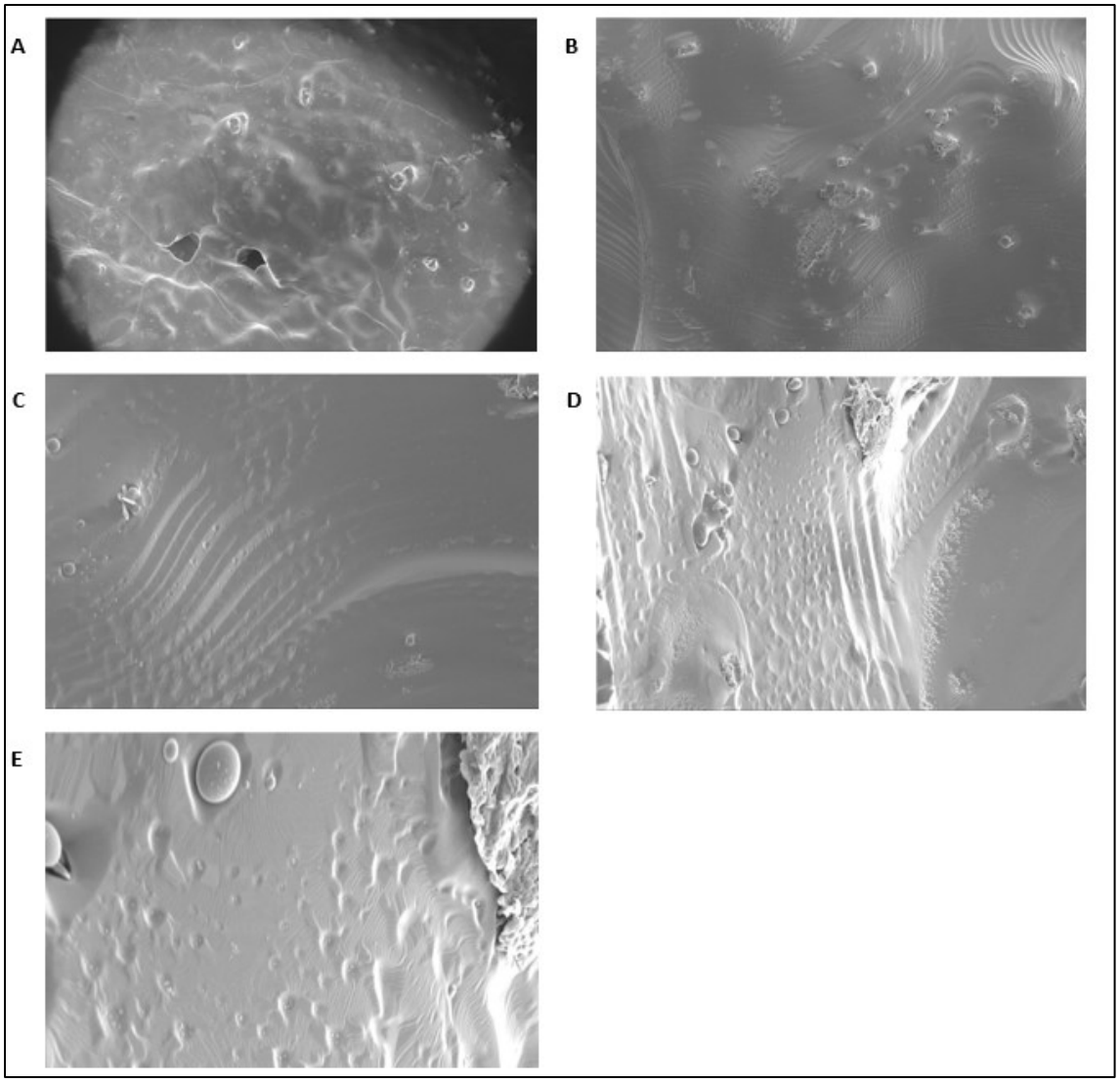

Figure 41 *SEM of sintered SDS-containing salt structure with magnifications of A) 99X, B) 561X, C) 2410X, D) 3650X, and E) 12840X.*

In the SEM image Figure 41 A, holes can be seen in the structure where entrapped air may have emerged to the surface during the sintering process. B and C shows a much smoother surface than of the structure containing AOT. One reason could be the much greater amount of surfactant and paraffin oil present in the SDS-containing pastes. Generally, it is more difficult to identify individual salt grains in the SDS-containing structures.

4.4.2 SEM of inorganic structures

SEM images were taken to evaluate crosscuts of the inorganic structures containing different sized particles. The evaluated specimens presented below are “IO1 1000”, “IO1 280”, “IO1 80”, “IO2 1000”, “IO2 280”, and “IO2 80”. In Figure 42 the differences of the crosscuts between these specimens can be seen.

Figure 42 *Crosscuts of IO1 (left) & IO2 (right) bars containing different sized particles. Desired particle sizes from top to bottom: 80, 280, 1000.*

A clear difference can be observed in shape fidelity between the bars prepared with different sized particles (Figure 42). All bars except “IO2 1000” in the bottom right corner were printed with a 1.51 mm nozzle. The ones containing particles 1000 has retained their shape well after the post-process, while the bars of 280 and 80 have collapsed or merged. As proven by the rheological measurement, pastes containing larger particles and a broader distribution of different sized particles flows easier, which could be a reason to this behavior of the bars. Another possibility is that the merging occurs because of unoptimized amounts of components in the paste, which affects the post-processing of the structures. In Figure 43 below, a closer look at the crosscuts of the 1000 bars are shown.

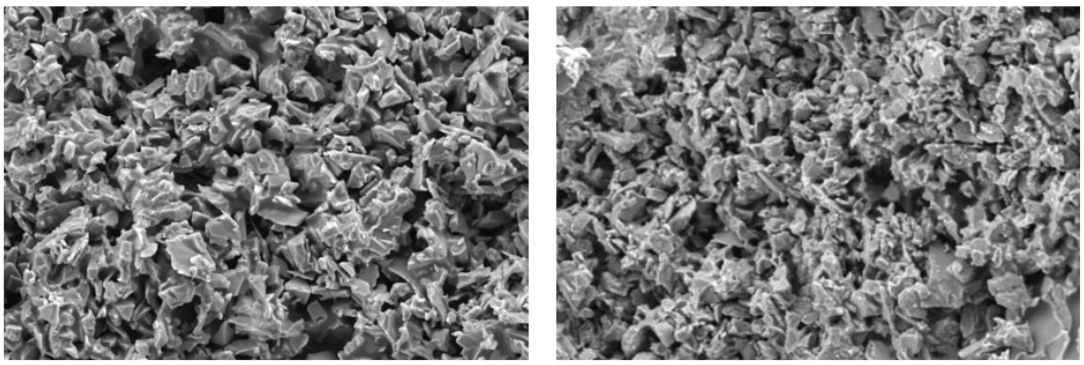

Figure 43 *SEM crosscut images of "IO1 1000" (left) and "IO2 1000" (right) at 1000X magnification.*

As expected, no major differences in the sizes of the particles can be observed for the bars of particles 1000 (Figure 43). The images were taken with different magnifications, thus the IO1 structure appears to have slightly larger particles. In Figure 44 below, a similar comparison of the bars containing particles 80 is shown.

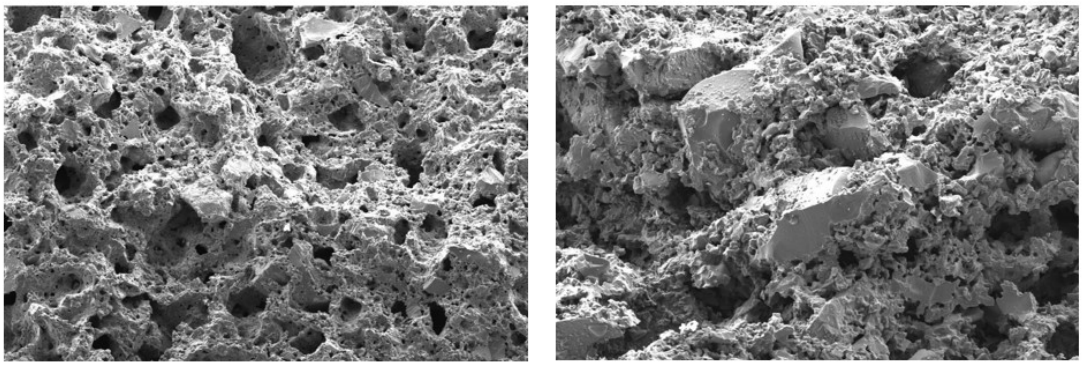

Figure 44 *SEM crosscut images of "IO1 80" (left) and "IO2 80" (right). "IO1 80" at 50X, and "IO2 80" at 140X magnification.*

In this comparison, the different sized particles can be seen in the structures (Figure 44). As for the comparison of the 1000 bars, these images were taken with different magnifications. The IO1 structure on the left shows a broader view of the surface of the crosscut, which appears quite porous, while in the image of the IO2 structure on the right the different sized particles appear clearer.

4.5 4-Point Bending mechanical strength test

Mechanical strength testing was performed on printed and post-processed inorganic bars with a 4-point bending test. The bars were all printed in the same size with a length of 60 mm, width of 10 mm, and a height of 6 mm. As reference samples, four conventionally manufactured bars were used. For each successfully printable inorganic paste, 1-3 bars were printed, post-processed, and tested. The speed of the bending test was set to 0.1 mm/min. In table 4 below, the results of the bending test are presented.

Table 4 4-Point Bending test results for bars of different components.

Name	Max force [N]	Bending strength [Mpa]	Bending strain [%]	Thickness [mm]	Width [mm]
Ref IO1 1	342.669	39.2501	0.1645	5.28	10.09
Ref IO1 2	341.39	39.4016	0.15469	5.26	10.09
IO1 - 1000 1	214.381	20.7983	0.3501	5.74	10.08
IO1 - 1000 2	376.466	32.7818	0.38799	6.02	10.21
IO1 - 400 1	404.63	35.464	0.28153	5.98	10.28
IO1 - 400 2	423.326	38.3647	0.26297	5.83	10.46
IO1 - 280 1	147.345	14.1324	0.20156	5.77	10.09
IO1 - 280 2	172.721	15.025	0.2065	5.84	10.86
IO1 - 280 3	165.684	14.907	0.24175	5.84	10.5
IO1 - 280 1*	393.142	37.0138	0.25874	5.85	10
IO1 - 280 2*	410.911	38.5849	0.22265	5.8	10.2
IO1 - 280 3*	398.835	35.6563	0.26292	5.95	10.18
IO1 - 280 1***	288.351	28.311	0.20098	5.72	10.03
IO1 - 150 1*	242.305	19.1805	0.1699	6.25	10.42
IO1 - 150 2*	334.78	30.012	0.20804	5.89	10.36
IO1 - 100 1*	162.95	9.38663	0.61917	7.07	11.19
IO1 - 80 1*	46.5028	2.441	0.23555	7.29	11.55
Ref IO2 1	392.294	32.5239	0.24813	6.2	10.11
Ref IO2 2	416.446	34.5604	0.22902	6.2	10.1
IO2/AOT - 1000 1	342.163	25.7049	0.28467	6.51	10.12
IO2/AOT - 1000 2	215.08	18.5531	0.17655	5.97	10.48
IO2 - 1000 1	130.921	14.5213	0.28653	5.45	9.78
IO2 - 1000 2	185.04	19.6614	0.22113	5.54	9.88
IO2 - 400 1	214.43	15.6368	0.33742	6.14	11.72
IO2 - 400 2	201.8	18.5631	0.26293	5.86	10.2
IO2 - 280 1	160.169	14.8639	0.23533	5.82	10.25
IO2 - 280 2	166.971	14.797	0.23989	5.89	10.48
IO2 - 280 1*	206.566	18.2684	0.21821	6	10.12
IO2 - 280 2*	193.872	17.6752	0.23062	5.93	10.05
IO2 - 150 1*	171.209	15.5734	0.21679	5.87	10.28
IO2 - 150 2*	150.222	13.8285	2.05494	5.94	9.92
IO2 - 100 1*	147.436	13.7497	0.26571	5.84	10.13
IO2 - 100 2*	193.249	19.13	0.21066	5.66	10.16
IO2 - 80 1*	160.321	14.8361	0.32014	5.8	10.35
IO2 - 80 2*	175.605	16.5626	0.2044	5.81	10.12

No markings = only the mentioned particle size used in the paste.

“ * ” = 50% of mentioned particle size + an even distribution of smaller particles.

“ *** ” = 50% of particle size 280 + 50% of particle size 1000.

As seen in table 4 above, none of the 3D printed bars possesses as high bending strength as the conventionally manufactured reference bars. However, a few of the printed bars comes close to the bending strength of their respective reference samples. It must be taken into consideration that a lot more problems arise during the printing process where weak spots may appear in the bars, compared to the conventional manufacturing process. These weak spots can be caused by air bubbles in the paste, inconsistent extrusion, inappropriate layer heights, nozzle cloggage, poor infill, etc. Therefore, the bars with nearly as high bending strength as the reference samples indicates a potential for the application of 3D printing in the relevant field.

Figure 45 below shows the bending strengths of the bars tested with 4-point bending. In the graph the differences between inorganic material used is easier to visualize.

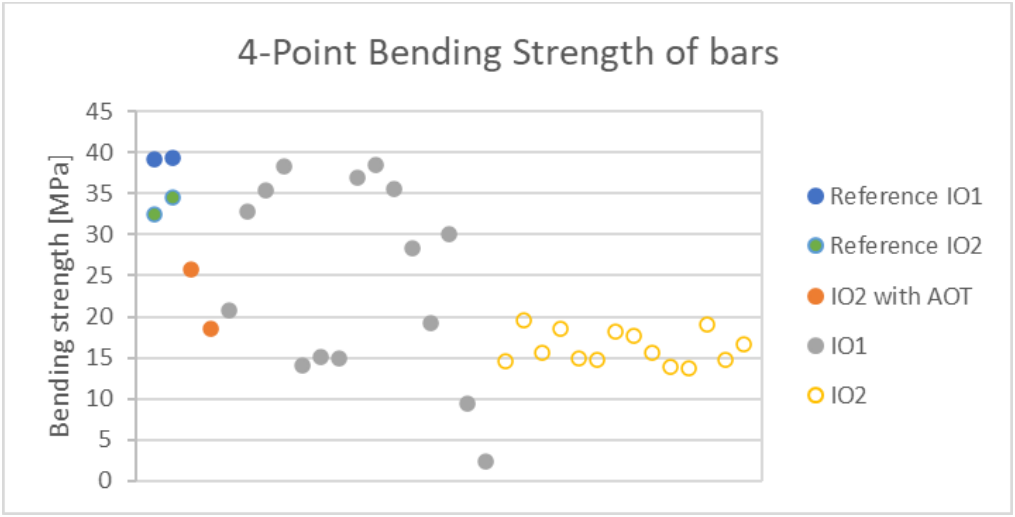

Figure 45 *Bending strength of different bars.*

As presented in the graph, bars containing the IO1 material generally has a higher bending strength than the ones containing the IO2 material. The IO2 bars did not reach as high bending strengths but are more consistent in strength. The two IO2 bars containing AOT shows above average strengths, but due to the lack of printability of pastes containing AOT, no further experiments were conducted.

There are apparent differences in strength depending on which inorganic material is used, but even greater differences between bars of the same material but with different particle distributions and sizes. In figures 46 and 47 below, the material specific differences are presented.

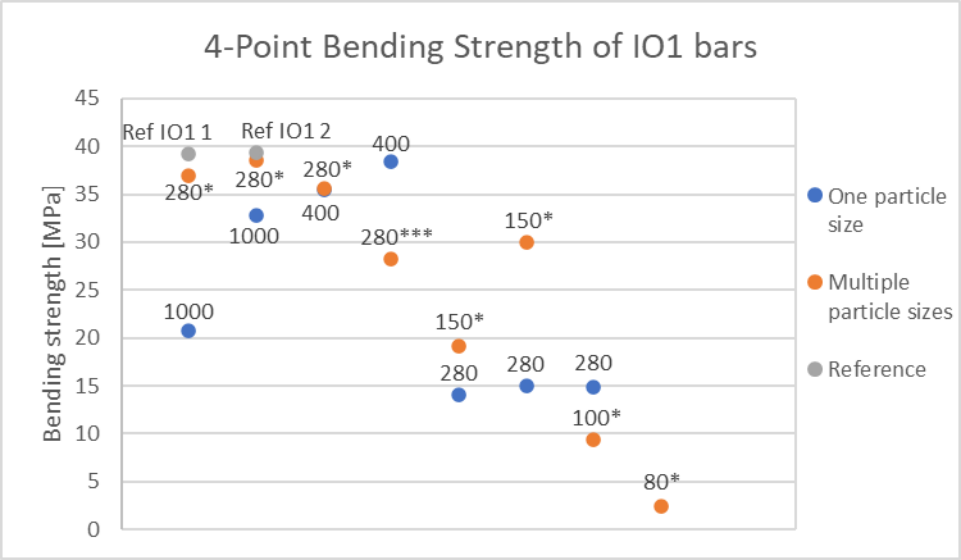

Figure 46 *Bending strength of IO1 bars with different particle sizes.*

Although a pattern of a decrease in bending strength with increasing particle sizes in the different pastes can be seen, there was a clear difference in flowability of the pastes of different compositions (Figure 46). The required printing pressure decreased for bars of larger particles with a broader particle size distribution, which means that an increase of solids in the paste would be possible. The bars containing larger particles shrunk more than the ones with smaller particles, thus an increase of solids could result in a decreased and more homogenous shrinkage, which most likely would result in improved bending strengths. A few of the printed bars have fairly similar bending strengths as the reference samples of the same IO1 material.

Four of the bars containing solely one particle size, 1000 or 400, shows proper bending strengths. However, the best comparison occurs between the different 280 particle-sized bars. The 3 bars marked as “280” in Figure 46 only contained particles of size 280 and shows relatively poor bending strengths compared to the ones marked as “280*” and

"280***", which contained a mixture of different particle sizes. Thus, it can be concluded that by broadening the size distribution, the strength of the bars improves. It also occurs that the "280*" bars, containing 50% of 280 particles and 16.67% of 400, 600, and 1000 particles, have better bending strengths than the "280***" bar, containing 50% of 280 and 50% of 1000 particles. By further optimizing the size distribution of particles present in the pastes, improved strengths could possibly be obtained. By evaluating rheology of the pastes and bending strengths of the bars, it can be concluded that the use of multiple particle sizes improves flowability and printability of the pastes, and strength of the bars.

By evaluating the differences in width and thickness of the bars, the "100*" and "80*" IO1 bars are much wider and thicker than the rest of the bars. As all bars have been printed with the same dimensions of 10x6x60 mm, it is surprising that these bars are much larger. Assumably, a wider and thicker structure would increase the bending strength, which is not the case. However, all the bars of particle sizes 100 or 80 of both "IO1" and "IO2" stuck to the platform during the post-processing stage, indicating a too liquid-like paste and yet another indication of the possibility of increasing the solids in these pastes. The removal of the bars from the platform may have affected the strength of the bars, decreasing the reliability of the measurement results. No other bar had any sticking issues during post-processing.

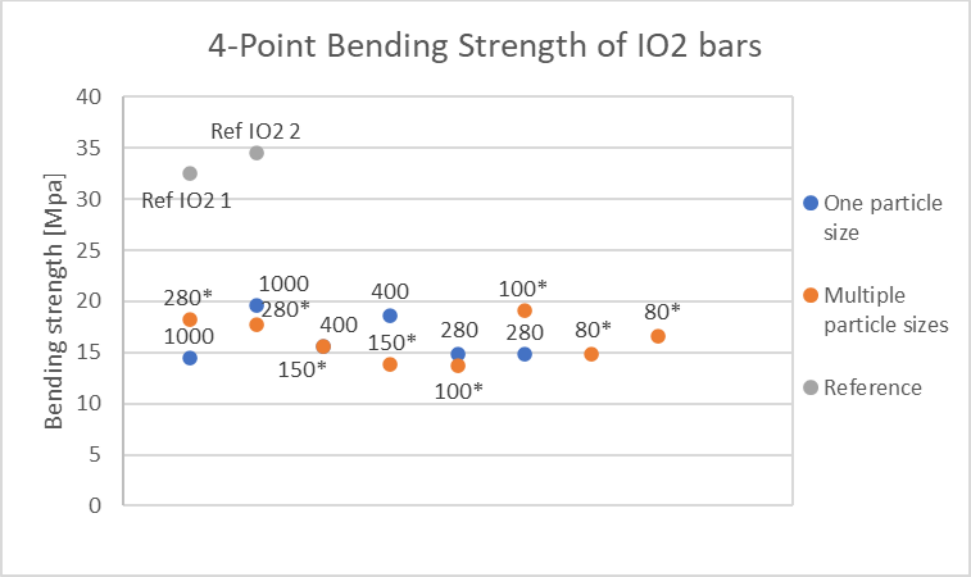

Figure 47 *Bending strengths of IO2 bars with different compositions.*

The bars containing the IO2 material shows much more consistency in the bending strengths compared to the IO1 bars. However, a similar pattern can be observed as the bars with a mixture of particle sizes generally have a higher bending strength than the ones containing only one particle size (Figure 47). None of the bars have bending strengths near the strengths of the reference bars, which could be a result of weak spots occurring in the printing process. The IO2 bars does not reach bending strength values near the reference samples of the same material.

As mentioned before, bars containing the largest particles, 100 and 80, stuck to the platform during the post-processing stage. As no apparent decrease in strength can be observed for these particular particle-sized bars of IO2 material, they have probably not been damaged when removed from the platform.

5 Conclusions

The main aim for this thesis was to evaluate the possibilities and drawbacks of 3D printing inorganic structures for industrial applications using DIW technology. This included preparation of different pastes of different components, evaluation and optimization of printing settings and parameters, and evaluation of post-processed 3D printed structures. The realization of the work was carried out in two separate experiments where the first part of the work consisted of recreating and printing a salt paste as described in the article "3D Printing of Salt as a Template for Magnesium with Structured Porosity" by Kleger et al. (2019). This was done to get familiar with the manufacturing process, as well as to confirm that 3D printing of inorganic materials was possible. For the second part of the work, the main part of the thesis, the salt was replaced by a mixture of inorganic particles. For both experiments, the primary objective was to maximize the proportion of inorganic material in the paste.

For the prepared pastes, rheology measurements were performed to investigate their behavior regarding flow and recovery. For the 3D printing process, parameters and settings, as well as different substrates and conditions were evaluated to optimize the process. For the post-processed structures, visual and mechanical measurement were performed.

From the salt experiment it was concluded that AOT is beneficial to maximize the proportion of salt in the pastes. This is due to the smaller required amount of surfactant and paraffin oil in the AOT-containing pastes, which allows greater solids loadings. By using AOT as surfactant, a paste was successfully prepared and printed with a salt concentration of approximately 83 wt-%. Salt structures were printed on filter paper, which immediately started to absorb the oil from the structure. Graphite powder was used to enhance drying of the structures, and to allow free contraction as the structures shrunk during the sintering process. This also prevented the structures from sticking to the platform.

The original idea for the main experiment was to utilize the working recipe for salt pastes and only replace the salt with a mixture of inorganic particles. This approach did not work, probably since a similar interaction between the sulfate groups in the surfactants and the

salt did not occur for the inorganic particles. As a result, the components of the paste separated during the 3D printing process. As an alternative approach, the binder consisting of surfactants and oil was replaced with a new binder, binder A. The advantages of this approach were that the binder A does not require chemical interactions. With binder A, well-dispersed inorganic pastes could easily be prepared by speed mixing the binder and the inorganic particles.

Different particle sizes of the inorganic materials were used in the preparation of different pastes. Initially, pastes containing only particles of one size were prepared, but as the particle size increased, the extrusion of the paste became inconsistent and uneven. To obtain a consistent and smooth extrusion, an attempt to mix particles of different sizes was done. This allowed a smooth extrusion of all particle sizes available for the work. Rheological evaluations of pastes with a distribution of different sized particles showed that pastes containing larger particles flows more easily than pastes of smaller particles. The particle size distribution in the pastes consisted of 50% of the desired particle size, along with an even distribution of particles smaller than the desired one. Thus, the larger the desired particle size, the wider the distribution of smaller sized particles present in the paste.

Inorganic structures were printed on aluminum foil, as this substrate provided enough adhesion for the structure to be printed on, but not too much to prevent detachment of the dried structures. The structures were printed with a nozzle with a diameter of 1.55 mm, allowing higher solids loadings in the pastes, at the cost of deteriorating resolution of the printed structures. Successfully printed and post-processed structures were obtained with approximately 75 wt-% of solids.

Pastes containing different sized inorganic particles were successfully prepared, printed, and post-processed. A few of the inorganic structures showed promising results in terms of strength and toughness and will be tested for industrial applications. Pastes with approximately 75 wt-% of solids were printable, with the possibility of a slight increase of inorganic content. By further optimizing the paste, a greater amount of solids could be achieved.

6 Swedish summary – Svensk sammanfattning

3D-printning av oorganiska material för industriella applikationer

3D-printning är en additiv tillverkningsmetod som tillämpas för att skapa fysiska objekt med komplexa geometrier (Chen et al., 2019). Objekten designas och skivas i tvådimensionella X-Y-tvärsnitt med hjälp av ett datorstött konstruktionsprogram (CAD) och printas enligt de skivade sektionerna ett lager i taget. 3D-printning möjliggör tillverkning av exakta och krävande strukturer som är svåra att tillverka med traditionella tillverkningsmetoder, samt ökar produktiviteten eftersom flera strukturer kan tillverkas samtidigt. Förutom ökad produktivitet erbjuder 3D-printning lösningar för olika utmaningar förknippade med de traditionella tillverkningsmetoderna, såsom höga kostnader, långa bearbetningstider och tillverkning av komplexa strukturer och geometrier med sammankopplade hål. En stor utmaning vid tillverkning av oorganiska strukturer är att producera porösa strukturer (Zhang et al., 2022). För att erhålla dessa porösa strukturer vid tillämpning av de traditionella tillverkningsmetoderna krävs ytterligare tillverkningssteg, vilket kan undvikas med 3D-printning.

3D-printning av oorganiska partiklar introducerades på 1990-talet (Chen et al., 2019). Sedan dess har många 3D-printningstekniker utvecklats i syfte att producera oorganiska strukturer. Dessa teknologier kan kategoriseras baserat på fasen av det förbearbetade råmaterialet i slambaserade, pulverbaserade och fasta bulkbaserade metoder. De additiva tillverkningsmetoderna är ytterligare kategoriserade i sju grupper baserat på råvarans initialtillstånd, appliceringsprocessen och härdningsprincipen. (Mamatha et al., 2022). Dessa sju grupper av additiv tillverkning klassificeras som materialextrudering, materialsprutning, polymerisation, pulverbäddfusion, arklaminering, bindemedelssprutning och riktad energideponering.

För denna avhandling ligger det huvudsakliga intresset inom ramen av materialextrudering med fokus på den slambaserade DIW-tekniken (eng. Direct ink writing technology). Målet med avhandlingen var att utvärdera möjligheterna och begränsningarna för 3D-printning av oorganiska material för industriella applikationer. Arbetet utfördes i två skilda experiment där den första delen av arbetet bestod av att återskapa en saltpasta tillverkad för 3D-printning så som den beskrivs i artikeln ”3D

Printing of Salt as a Template for Magnesium with Structured Porosity" av Kleger et al., (2019). Detta gjordes för att få en uppfattning om tillverkningsprocessen i sin helhet, samt bekräftelse att 3D-printning av ett oorganiskt material är möjligt. För det andra experimentet, den viktigaste delen i avhandlingen, byttes saltet mot en blandning av oorganiska partiklar. För de båda undersökningarna var det primära målet att maximera andelen oorganiskt material i pastorna.

Båda undersökningarna som utfördes i denna avhandling bestod av tillverkning av pastor med olika komponenter i olika förhållanden, 3D-printning av dessa pastor och efterbehandling av de 3D-printade strukturerna. Lämpliga mätningar och evalueringar under olika skeden av processen utfördes för att erhålla en bred uppfattning om processen i sin helhet. För de tillverkade pastorna utfördes reologimätningar för att undersöka deras beteende gällande flöde och återhämtning, för 3D-printningen evaluerades och undersöktes parametrar och inställningar samt olika underlag och förhållanden för att optimera processen och för de färdiga efterbehandlade strukturerna utfördes visuella och mekaniska mätningar.

Det första experimentet utfördes med saltpastor som bestod av NaCl, någondera av surfaktanterna SDS och AOT samt paraffinolja. De pastor som tillverkades med SDS kunde tillverkas i en kulkvarn genom att mala alla komponenterna på en gång, medan pastorna som tillverkades med AOT krävde ett ytterligare steg i tillverkningen som bestod av att lösa upp surfaktanten i paraffinoljan med magnetisk omrörning. För båda pastorna visade det sig fördelaktigt att mala saltkornen skilt till små partiklar för att minska risken för tilltäppning av munstycket under 3D-printningen. Pastornas beteende undersöktes med hjälp av amplitudsvep och tixotropitest i tre intervaller, utifrån vilka pastorna visade ett skjuvtunnande beteende och en mycket snabb återhämtning, vilket är optimalt för 3D-printning med DIW-tekniken. Mätningarna tydde på att användning av surfaktanten AOT är fördelaktig då den tillåter en större andel NaCl i pastorna. Den maximala andelen NaCl som erhölls i en för 3D-printning fungerande pasta låg kring 83 viktprocent.

3D-printning av saltpastorna utfördes på ett filterpapper för att absorbera paraffinoljan ur strukturerna direkt efter extrudering och därmed effektivera torkningen av strukturerna. Beroende på mängden salt i pastorna behövde tryck, hastighet och munstyckets diameter justeras för att erhålla en kontinuerlig och jämn utmatning av de olika pastorna.

Torkningen av de 3D-printade strukturerna effektiverades ytterligare genom att täcka dem med grafitpulver. Grafitpulver användes även under efterbehandlingsprocessen för att tillåta fri sammandragning av strukturerna då de krympte i sintringsugnen, samt som underlag för att förhindra strukturerna från att fastna i sintringsplattan.

Sintringen av de 3D-printade saltstrukturerna utfördes över ett uppvärmningstidsintervall på 19 timmar, följt av naturlig kylning till rumstemperatur. Under uppvärmningen till sintringstemperaturen 690°C ingick två uppehållstider vid 200°C respektive 400°C. Den första uppehållstiden varade i två timmar, under vilka paraffinoljan avlägsnades. Den andra uppehållstiden varade i fyra timmar där surfaktanterna förbrändes. Själva sintringen av saltstrukturerna varade totalt tre timmar.

För den huvudsakliga undersökningen i avhandlingen byttes saltet ut mot en blandning av oorganiska partiklar. Den ursprungliga idén för undersökningen var att utnyttja de fungerande recepten för saltpastor och byta ut saltet mot den oorganiska materialblandningen. Detta tillvägagångssätt fungerade inte då en liknande interaktion mellan sulfatgrupperna i surfaktanterna och saltet inte verkade förekomma för de oorganiska materialen. Som följd av detta separerade komponenterna i pastan under 3D-printningsprocessen. Som alternativt tillvägagångssätt ersattes bindemedlet av surfaktanter och paraffinolja med ett nytt bindemedel. Fördelen med det nya bindemedlet var att det fungerade utan kemiska interaktioner.

Framställningen av oorganiska pastor skedde genom att tillsätta blandningen av oorganiska material till bindemedlet och blanda om komponenterna med en höghastighetsmixer. Efter processen erhölls en väl omblandad dispersion som uppvisade ett skjuvtunnande beteende och en mycket snabb återhämtning.

Olika partikelstorlekar av de oorganiska materialen användes vid framställningen av de olika pastorna. Till en början framställdes pastor som enbart innehöll partiklar av en storlek, men då partikelstorleken ökade framträdde problem under 3D-printningsprocessen i form av ojämn utmatning av pastan. För att erhålla en konsekvent utmatning och en välflytande pasta gjordes ett försök att blanda partiklar av olika storlekar i samma pasta. Detta möjliggjorde extrudering av alla storlekar av partiklar tillgängliga för arbetet. Reolologiska evalueringar av pastor med en distribution av olika

partikelstorlekar visade att pastorna som innehöll större partiklar flöt lättare än pastor av mindre partiklar. Utifrån resultaten kunde slutsatsen dras om att pastor med en större distribution av partiklar flyter lättare och kräver lägre tryck vid extrudering.

Partikelstorleksfördelningen i pastorna bestod till 50 % av den önskade partikelstorleken tillsammans med en jämn fördelning av partiklar mindre än den önskade storleken. Detta innebar att ju större den önskade partikelstorleken var, desto bredare blev distributionen av partiklar av mindre storlek i pastan.

3D-printning av de oorganiska pastorna utfördes på aluminiumfolie, eftersom filterpapper inte fungerade på samma vis som för saltpastorna. Vid kontakt mellan den oorganiska pastan och filterpappret började filterpappret skrynkla ihop sig. Med aluminiumfolie var vidhäftningen mellan den 3D-printade strukturen och underlaget tillräcklig för att bygga upp strukturen utan problem, men inte för effektiv för att förhindra losstagning av strukturerna då de torkat. För 3D-printning av de oorganiska strukturerna användes ett munstycke med en diameter på 1,51 mm. Fördelarna av ett större munstycke är att pastor med högre andel oorganiskt material kan extruderas och processen förlöper snabbare. Nackdelen med ett större munstycke är att resolutionen av strukturerna försämras. Exempelvis får skarpa hörn en mer avrundad form, men för de runda strukturerna som tillverkades i detta experiment var resolutionen tillräcklig och därmed var ett större munstycke fördelaktigt. Andelen oorganiskt material som tillsattes i pastorna låg kring 75 viktprocent, men en ökning ansågs vara möjlig för pastorna som innehöll partiklar av de största storlekarna. Detta antagande baserade sig på att dessa pastor flöt lättare och kunde extruderas med lägre tryck.

Efterbehandlingen av de 3D-printade oorganiska strukturerna var betydligt enklare än för saltstrukturerna i och med att de oorganiska strukturerna torkade i rumstemperatur utan tillsats av grafitpulver. Efter 1–2 dygn var strukturerna så torra att de kunde hanteras utan att förstöras och var därmed enkla att förflytta till plattan. För efterbehandlingen användes grafitpulver för att förhindra strukturerna att fastna i plattan under processen, samt för att tillåta fri kontraktion av strukturerna då de krymper. Inga märkbara defekter uppstod under efterbehandlingen.

Sammanfattningsvis har pastor av oorganiska partiklar kunnat tillredas och användas för 3D-printning. Alla pastor visade ett för DIW-processen idealt skjuvtunnande beteende med en mycket snabb återhämtning. Efterbehandlingsprocessen fungerade utan märkbara defekter i strukturerna. Ytterligare forskning för optimering av pastorna i fråga om förhållanden av komponenter och partikelstorleksdistribution rekommenderas för att erhålla en kontinuerligt jämnare extrusion och högre styrka i de efterbehandlade strukturerna. Efter optimering av pastorna bör krympningen av strukturerna evalueras för eventuell korrigering av CAD-modellerna.

7 References

Ang, X., Tey, J. Y., Yeo, W. H. & Shak, K. P. Y. 2023. A review on metallic and ceramic material extrusion method: Materials, rheology, and printing parameters. *Journal of manufacturing processes, 90*, pp. 28-42. doi:10.1016/j.jmapro.2023.01.077

Anton Paar GmbH. (2023) 3iTT test. Available at: https://wiki.anton-paar.com/en/3itt-test/ (Accessed: 11.05.2023).

Anton Paar GmbH. (2023) Amplitude sweep. Available at: https://wiki.anton-paar.com/ca-en/amplitude-sweeps/ (Accessed: 12.04.2023).

Anton Paar GmbH. (2023) Flow curve and yield point determination with rotational viscometry. Available at: https://wiki.anton-paar.com/en/flow-curve-and-yield-point-determination-with-rotational-viscometry/ (Accessed: 12.04.2023).

Anton Paar GmbH. (2023) Modular Compact Rheometer: MCR 702e. Available at: https://www.anton-paar.com/corp-en/products/details/rheometer-mcr-702-multidrive/ (Accessed: 06.10.2023).

Brinter. (2023) Brinter ONE – Multitool 3D bioprinter. Available at: https://www.brinter.com/product/brinter-one/ (Accessed: 11.09.2023).

CEM Corporation. (2006) Phoenix Microwave Muffle Furnace. Available at: http://www.cemmicroonde.it/Phoenix.pdf (Accessed: 06.10.2023).

Chaudhary, R., Fabbri, P., Leoni, E., Mazzanti, F., Akbari, R. & Antonini, C. 2022. Additive manufacturing by digital light processing: A review. *Progress in additive manufacturing*. doi:10.1007/s40964-022-00336-0

Chen, A., Wu, J., Liu, K., Chen, J., Xiao, H., Chen, P., Li, C. & Shi, Y. 2018. High performance ceramic parts with complex shape prepared by selective laser sintering: A review. *Advances in applied ceramics, 117*(2), pp. 100-117. doi:10.1080/17436753.2017.1379586

Chen, Z., Li, Z., Li, J., Liu, C., Lao, C., Fu, Y., Liu, C., Li, Y., Wang, P. & He, Y. 2019. 3D printing of ceramics: A review. *Journal of the European Ceramic Society, 39*(4), pp. 661-687. doi:10.1016/j.jeurceramsoc.2018.11.013

Cloitre, M. & Bonnecaze, R. T. 2017. A review on wall slip in high solid dispersions. *Rheologica acta, 56*(3), pp. 283-305. doi:10.1007/s00397-017-1002-7

Coffigniez, M., Gremillard, L., Balvay, S., Lachambre, J., Adrien, J. & Boulnat, X. 2021. Direct-ink writing of strong and biocompatible titanium scaffolds with bimodal interconnected porosity. *Additive manufacturing, 39*, p. 101859. doi:10.1016/j.addma.2021.101859

del-Mazo-Barbara, L. & Ginebra, M. 2021. Rheological characterisation of ceramic inks for 3D direct ink writing: A review. *Journal of the European Ceramic Society, 41*(16), pp. 18-33. doi:10.1016/j.jeurceramsoc.2021.08.031

Dermeik, B. & Travitzky, N. 2020. Laminated object manufacturing of ceramic-based materials. *Advanced engineering materials, 22*(9), pp. 2000256-n/a. doi:10.1002/adem.202000256

FlackTec, (2022) Small Speedmixers. Available at: https://speedmixer.com/speedmixers/small/ (Accessed: 22.05.2023).

FlackTek, (2022) The Technology. Available at: https://speedmixer.com/the-technology/ (Accessed: 22.05.2023).

Grossin, D., Montón, A., Navarrete-Segado, P., Özmen, E., Urruth, G., Maury, F., Maury, D., Frances, C., Tourbin, M., Lenormand, P., & Bertrand, G. 2021. A review of additive manufacturing of ceramics by powder bed selective laser processing (sintering / melting): Calcium phosphate, silicon carbide, zirconia, alumina, and their composites. *Open Ceramics, 5*, p. 100073. doi:10.1016/j.oceram.2021.100073

Hwa, L. C., Rajoo, S., Noor, A. M., Ahmad, N. & Uday, M. 2017. Recent advances in 3D printing of porous ceramics: A review. *Current opinion in solid state & materials science, 21*(6), pp. 323-347. doi:10.1016/j.cossms.2017.08.002

Kleger, N., Cihova, M., Masania, K., Studart, A. R. & Löffler, J. F. 2019. 3D printing of salt as a template for magnesium with structured porosity. *Advanced materials (Weinheim), 31*(37), pp. e1903783-n/a. doi:10.1002/adma.201903783

Mamatha, S., Biswas, P. & Johnson, R. 2022. Digital light processing of ceramics: An overview on process, materials and challenges. *Progress in additive manufacturing*. doi:10.1007/s40964-022-00379-3

Mohamed, O. A., Masood, S. H. & Bhowmik, J. L. 2015. Optimization of fused deposition modeling process parameters: A review of current research and

future prospects. *Advances in manufacturing, 3*(1), pp. 42-53. doi:10.1007/s40436-014- 0097-7

Saadi, M. A. S. R., Maguire, A., Pottackal, N. T., Thakur, M. S. H., Ikram, M. M., Hart, A. J., Ajayan, P. M. & Rahman, M. M. 2022. Direct ink writing: A 3D printing technology for diverse materials. *Advanced materials (Weinheim), 34*(28), pp. e2108855-n/a. doi:10.1002/adma.202108855

Santoliquido, O., Colombo, P. & Ortona, A. 2019. Additive manufacturing of ceramic components by Digital light processing: A comparison between the "bottom up" and the "top-down" approaches. *Journal of the European Ceramic Society, 39*(6), pp. 2140-2148. doi:10.1016/j.jeurceramsoc.2019.01.044

Vyavahare, S., Teraiya, S., Panghal, D. & Kumar, S. 2020. Fused deposition modelling: A review. *Rapid prototyping journal, 26*(1), pp. 176-201. doi:10.1108/RPJ 04-2019-0106

Zhang, F., Li, Z., Xu, M., Wang, S., Li, N. & Yang, J. 2022. A review of 3D printed porous ceramics. *Journal of the European Ceramic Society, 42*(8), pp. 3351-3373. doi:10.1016/j.jeurceramsoc.2022.02.039

Ziaee, M. & Crane, N. B. 2019. Binder jetting: A review of process, materials, and methods. *Additive manufacturing, 28*, pp. 781-801. doi:10.1016/j.addma.2019.05.031

8 Appendices

8.1 Appendix A – Rheology measurements of inorganic pastes

All pastes prepared with solids loadings of 75 wt-%. The binder A as reference sample.

Binder A

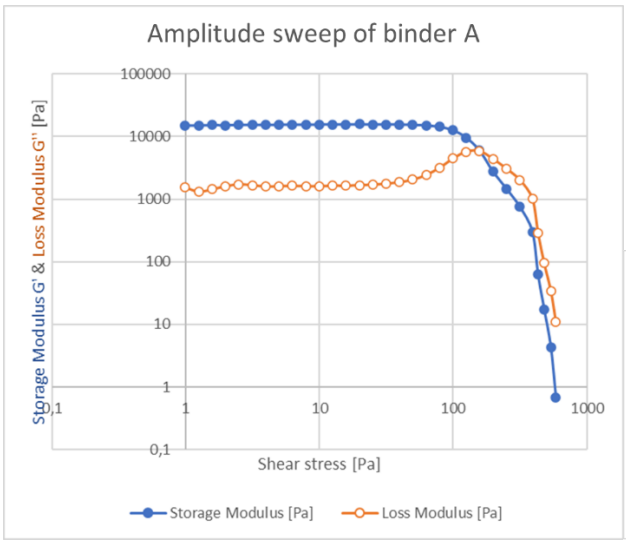

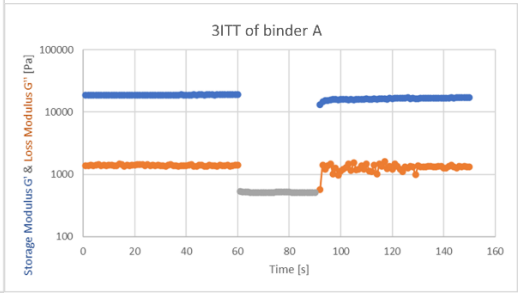

Binder A used in the inorganic pastes. Recovers rapidly after structural breakdown.

IO1 - 400

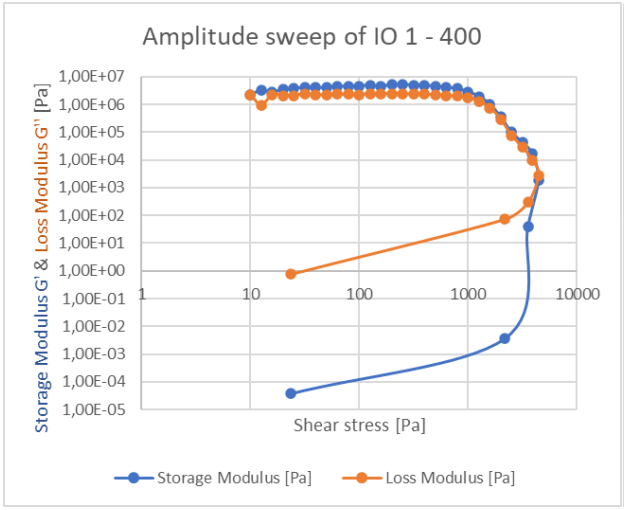

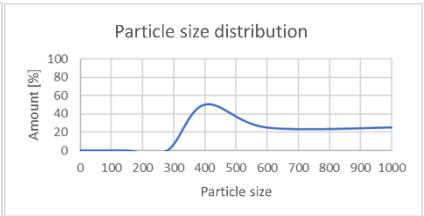

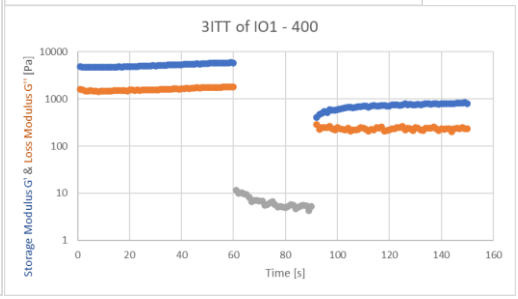

Particle sizes in paste: 400 (50%), 600 (25%), 1000 (25%). A narrow particle size distribution results in a less flowable paste. Thus, some inaccuracy occurs in the latter measurement points for the amplitude sweep. Paste recovers rapidly.

IO1 - 280

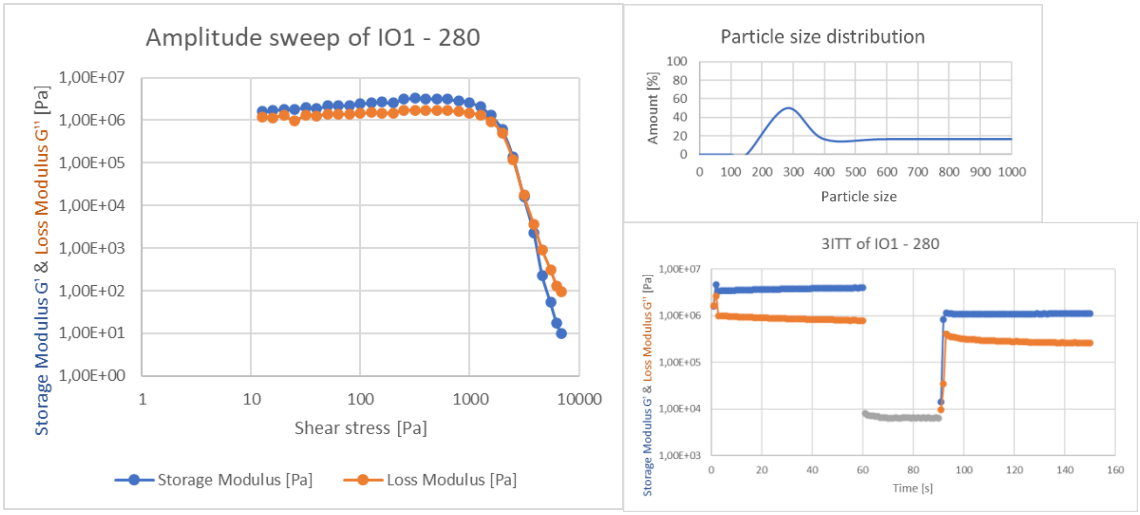

Particle sizes in paste: 280 (50%), 400 (16.67%), 600 (16.67%), 1000 (16.67%). As the particle size distribution increases, a clear improvement in the measurement accuracy is seen as the paste flows easier. The paste recovers almost instantly.

IO1 - 150

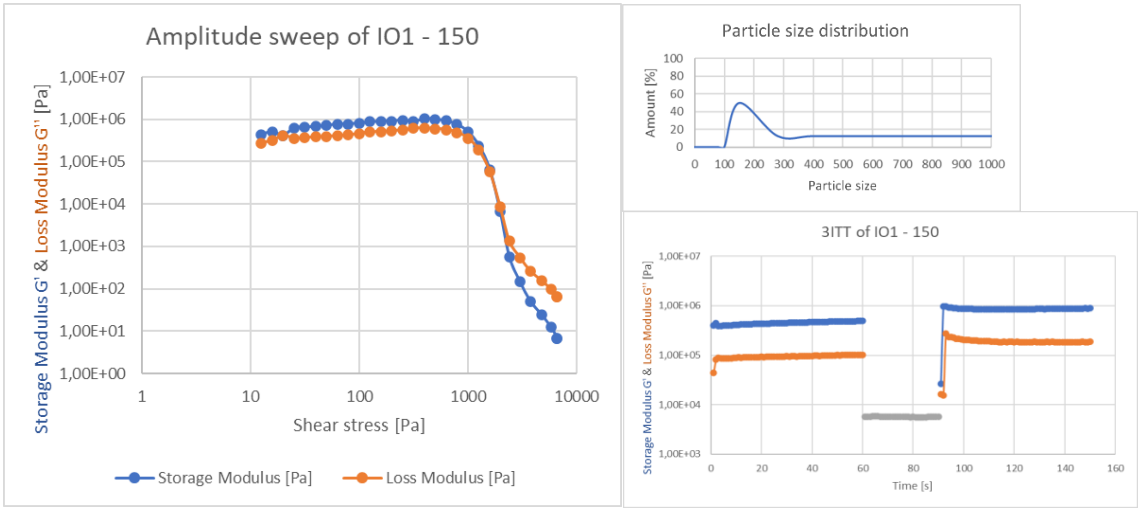

Particle sizes in paste: 150 (50%), 280 (12.5%), 400 (12.5%), 600 (12.5%), 1000 (12.5%). With an increased particle size distribution and larger particles present in the paste, the paste appears to recover completely almost instantly.

IO1 - 100

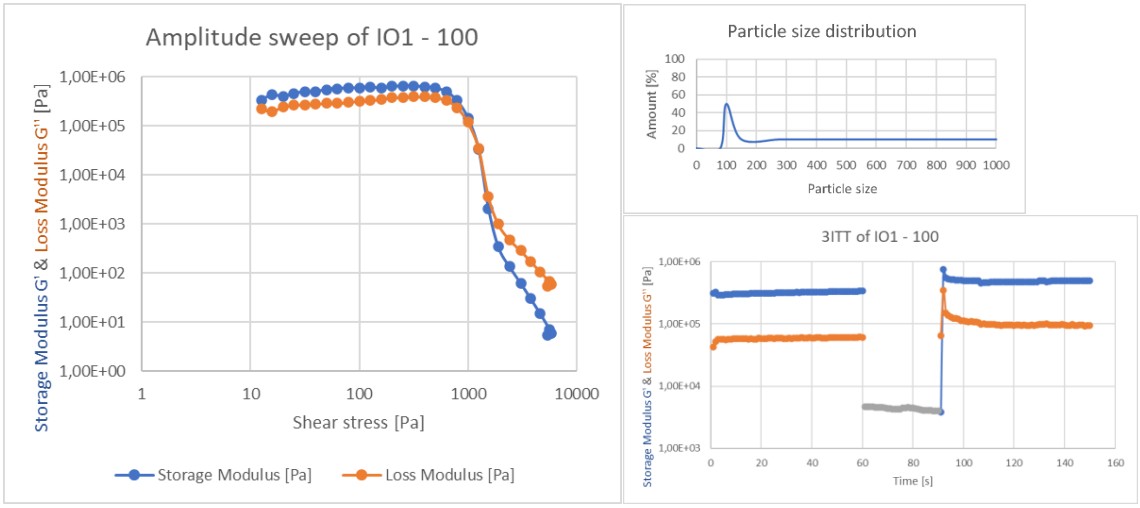

Particle sizes in paste: 100 (50%), 150 (10%), 280 (10%), 400 (10%), 600 (10%), 1000 (10%). Like the “IO1 150” paste, this paste seemingly recovers completely rapidly.

IO1 - 80

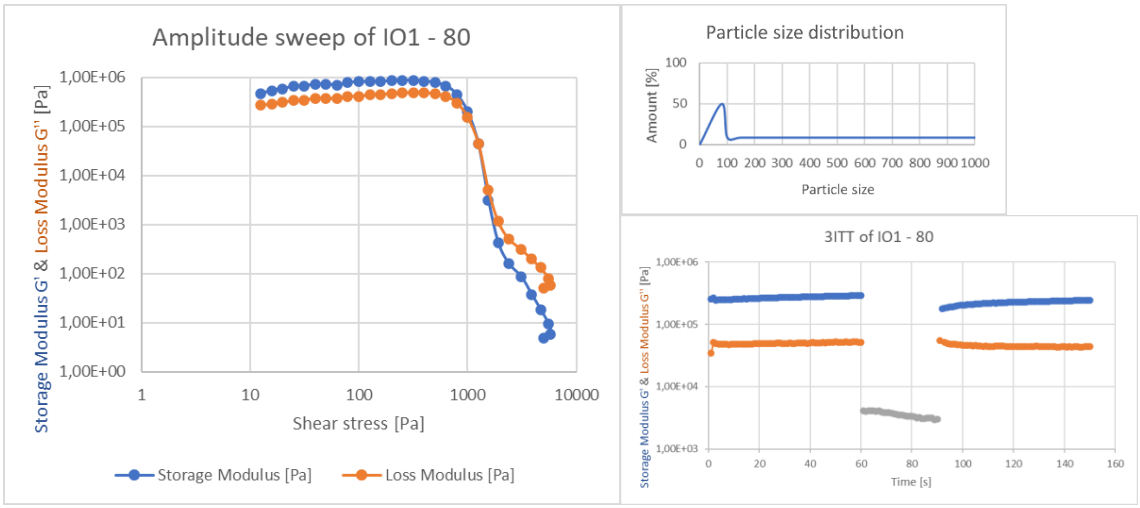

Particle sizes in paste: 80 (50%), 100 (8.33%), 150 (8.33%), 280 (8.33%), 400 (8.33%), 600 (8.33%), 1000 (8.33%). After structural breakdown, the paste recovers quickly.

Attempted measurements on a paste containing only particles of size 1000 did not provide any measurement points. With solids loadings of 75 wt-%, the paste is too thick. With decreasing storage and loss modulus by increasing particle sizes and a broader size distribution, the flowability of the pastes improves. The printability, with decreasing required shear stress due to a broader particle size distribution, and post-printed structures behavior indicates that greater solids loadings can be achieved with a broad particle size distribution (> 75 wt-%).

IO2 – 400

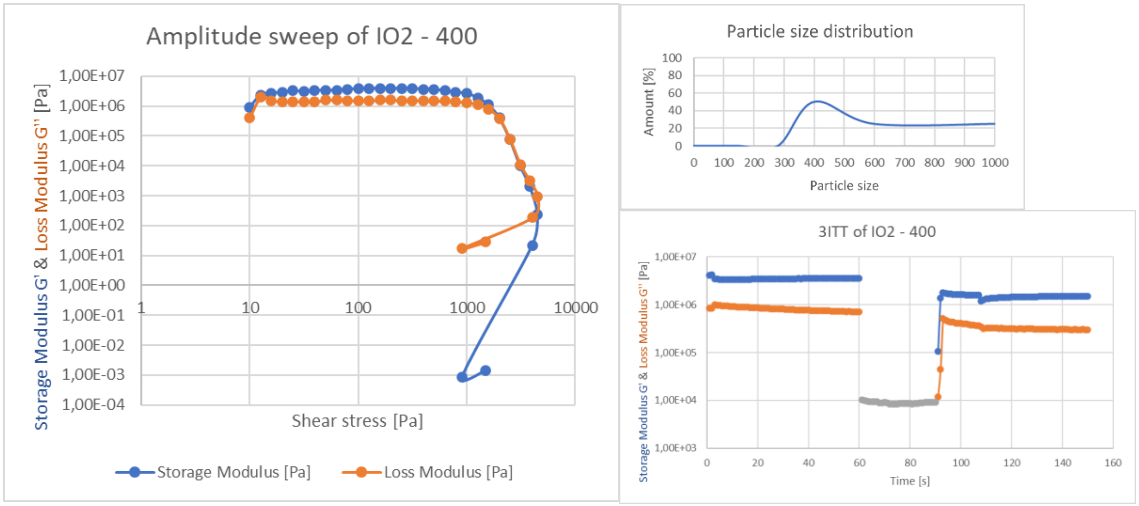

Particle sizes in paste: 400 (50%), 600 (25%), 1000 (25%). Like the “IO1 400” paste, a narrow particle size distribution results in a less flowable paste. Similar inaccuracy occurs in the latter measurement points for the amplitude sweep. Paste recovers rapidly.

IO2 – 280

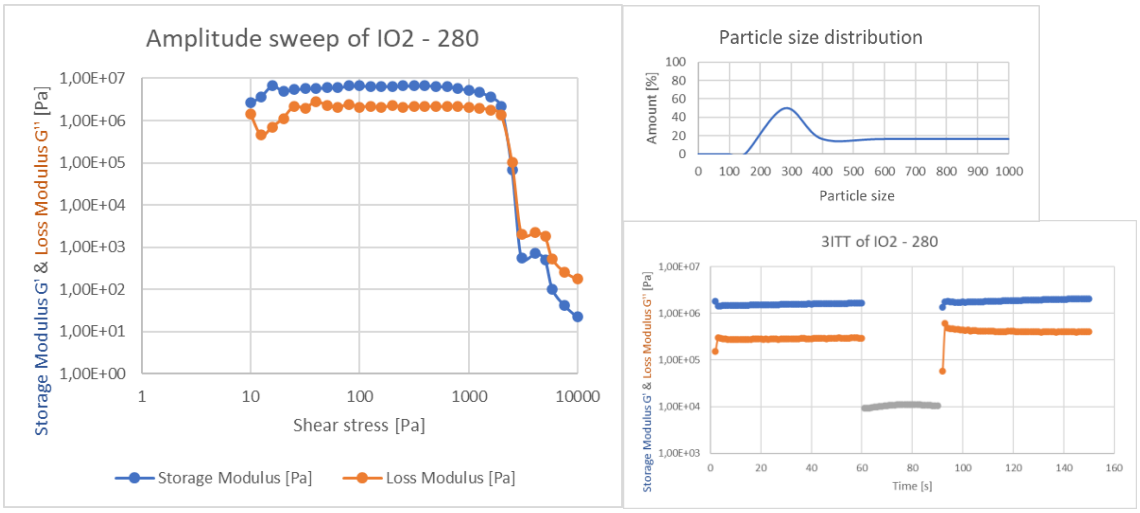

Particle sizes in paste: 280 (50%), 400 (16.67%), 600 (16.67%), 1000 (16.67%). Once again improvements in flowability and measurement accuracy can be seen as the particle size distribution broadens. Rapid complete recovery after structural breakdown.

IO2 – 150

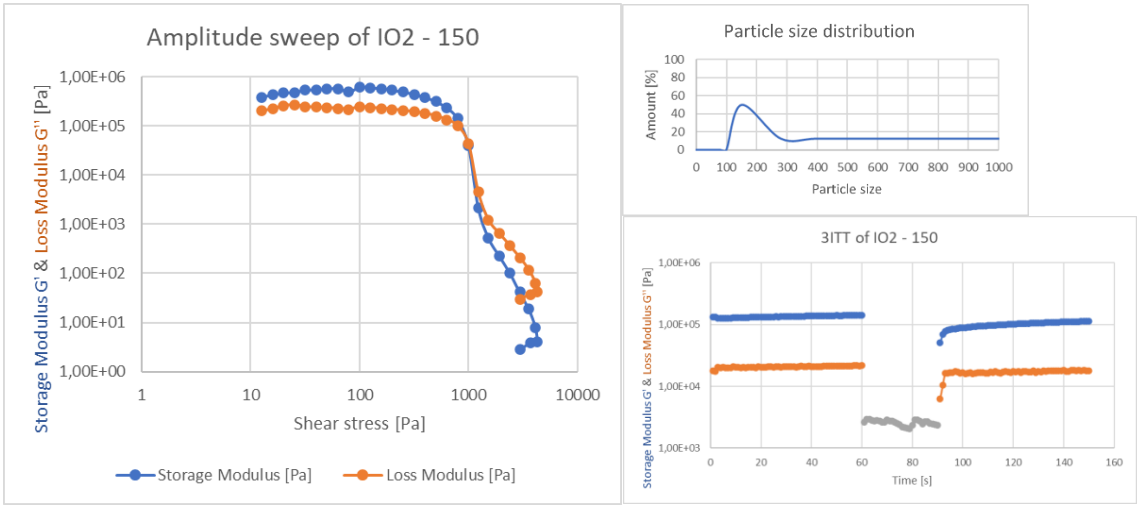

Particle sizes in paste: 150 (50%), 280 (12.5%), 400 (12.5%), 600 (12.5%), 1000 (12.5%). Like the results of the IO1 pastes, the required shear stress to flow decreases as the particle size distribution increases. The paste recovers rapidly.

IO2 – 100

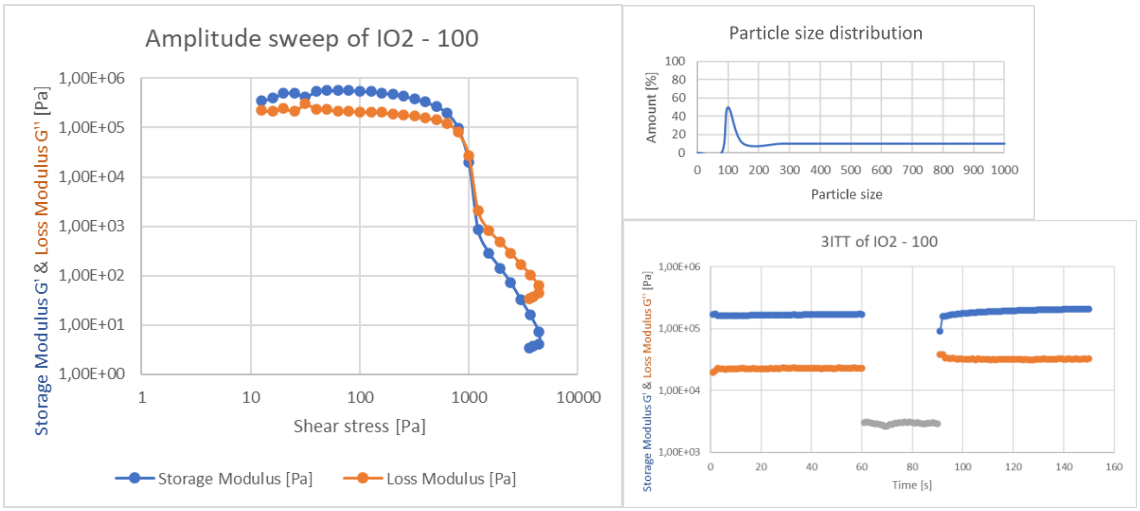

Particle sizes in paste: 100 (50%), 150 (10%), 280 (10%), 400 (10%), 600 (10%), 1000 (10%). The paste follows the same patterns with flowability at decreased shear stress. Recovers completely rapidly.

IO2 – 80

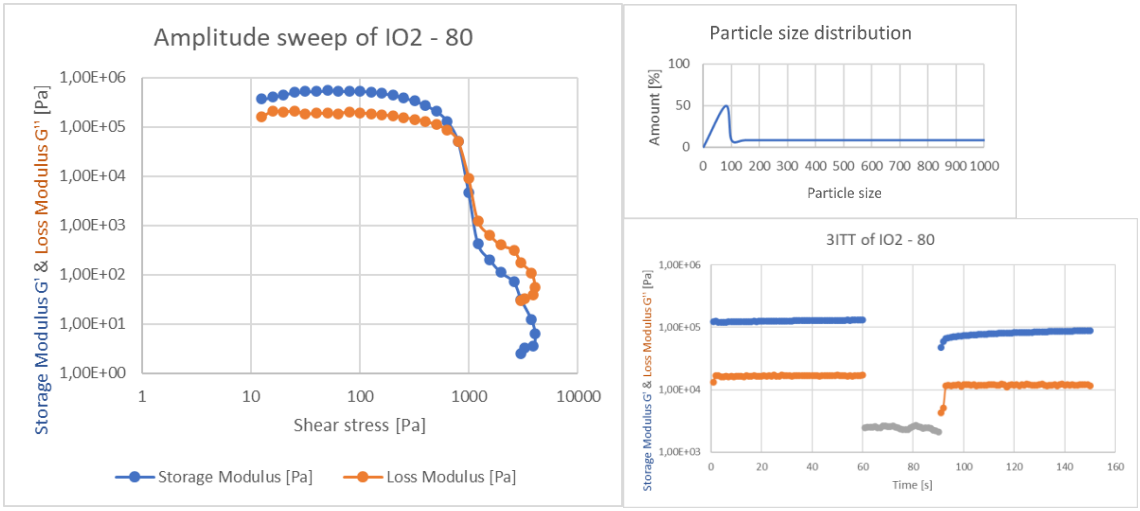

Particle sizes in paste: 80 (50%), 100 (8.33%), 150 (8.33%), 280 (8.33%), 400 (8.33%), 600 (8.33%), 1000 (8.33%). Same pattern as with the rest of the inorganic pastes. Improved flowability at lower shear stress and rapid recovery after structural breakdown.

Like the “IO1 1000” paste, no measurement points could be obtained for the IO2 paste containing only the smallest particle size 1000. With increasing size of particles and a broader size distribution, the flowability of each paste improved. A slight increase of solids could be possible for the pastes containing the largest particles, and a broad particle size distribution.